Continuum state spectroscopy: A high resolution ion imaging study of IBr photolysis in the wavelength range 440–685 nm

Eckart Wrede,[a] Stefan Laubach,[b] Sonja Schulenburg,[b] Alex Brown,[c] Eloy R. Wouters, Andrew J. Orr-Ewing, and Michael N. R. Ashfold
School of Chemistry, University of Bristol, Bristol BS8 1TS, United Kingdom

(Received 19 September 2000; accepted 9 November 2000)

The photodissociation of jet-cooled IBr molecules has been investigated at numerous excitation wavelengths in the range 440–685 nm using a state-of-art ion imaging spectrometer operating under optimal conditions for velocity mapping. Image analysis provides precise threshold energies for the ground, $I(^2P_{3/2})+Br(^2P_{3/2})$, and first excited $[I(^2P_{3/2})+Br(^2P_{1/2})]$ dissociation asymptotes, the electronic branching into these two active product channels, and the recoil anisotropy of each set of products, as a function of excitation wavelength. Such experimental data have allowed mapping of the partial cross-sections for parallel (i.e., $\Delta\Omega=0$) and perpendicular (i.e., $\Delta\Omega=\pm1$) absorptions and thus deconvolution of the separately measured (room temperature) parent absorption spectrum into contributions associated with excitation to the $A\,^3\Pi(1)$, $B\,^3\Pi(0^+)$ and $^1\Pi(1)$ excited states of IBr. Such analyses of the continuous absorption spectrum of IBr, taken together with previous spectroscopic data for the bound levels supported by the *A* and *B* state potentials, has allowed determination of the potential energy curves for, and (*R* independent) transition moments to, each of these excited states. Further wave packet calculations, which reproduce, quantitatively, the experimentally measured wavelength dependent product channel branching ratios and product recoil anisotropies, serve to confirm the accuracy of the excited state potential energy functions so derived and define the value (120 cm^{-1}) of the strength of the coupling between the bound (*B*) and dissociative (*Y*) diabatic states of 0^+ symmetry. © *2001 American Institute of Physics.*
[DOI: 10.1063/1.1337049]

I. INTRODUCTION

The fragmentation of IBr molecules following excitation in the visible wavelength region has long been a source of fascination to both experimentalists and theoreticians, not least of all because of the mixed adiabatic–diabatic picture required to interpret its spectroscopy and predissociation dynamics.[1,2] For future reference, Fig. 1 shows the diabatic/adiabatic correlation diagram of IBr and its separated fragments, illustrating the electronic configurations and molecular term symbols together with the labels of the electronic states of interest for this study. Early spectroscopic investigations identified two progressions of vibrational band heads in the near infrared (IR) and visible.[3] These were attributed to transitions from the $X\,^1\Sigma^+(0^+)$ ground state to, respectively, the $A\,^3\Pi(1)$ and $B\,^3\Pi(0^+)$ states resulting from a $\sigma^*\leftarrow\pi^*$ orbital promotion. Subsequent higher resolution studies[4–7] have served to confirm these assignments and to provide detailed information about the rovibrational level structure within the bound regions of these two excited state potentials, while analyses of the $B-X$ dispersed emission spectrum[8] and more recent high resolution far IR absorption measurements have led to a refined parameterization of the ground state rovibrational constants and potential energy function.[9] The bond dissociation energy, D_0(I–Br), first estimated by extrapolation of the observed sequence of band heads in the $A-X$ absorption system,[3] has recently been determined via direct, isotope selective, velocity mapping measurements of the ground state Br atomic fragments that result following excitation at energies just above the dissociation threshold.[10] The deduced thresholds for forming ground state products from both $I^{79}Br$ and $I^{81}Br$ molecules are consistent with an equilibrium value $D_e(I–Br)=14\,798\pm1$ cm^{-1}.

The minimum of the $B\,^3\Pi(0^+)$ state lies above this energy ($T_e=16\,168.4$ cm^{-1}),[7] but vibrational levels with $v'\leqslant3$ have been observed in fluorescence, albeit with fluorescence lifetimes that decrease with increasing v' and J', and are all substantially smaller than the estimated radiative lifetime of 3.9 μs.[7] *B* state levels with $v'>3$ predissociate much faster. The fluorescence quantum yield from these levels is thus too small to be detectable, but the $B-X$ absorption spectrum shows a progression of (diffuse) vibronic band heads converging to the first excited dissociation limit, associated with the products $I(^2P_{3/2})+Br(^2P_{1/2})$.[3] In a diabatic picture, the predissociation of levels with $v'>3$ is viewed as a consequence of a coupling between the bound $B\,^3\Pi(0^+)$ and repulsive $Y(0^+)$ state potentials in the vicinity of their crossing point on the outer limb of the *B* state well, at energies close to the $v'=5$ level of the diabatic *B* state. The alternative adiabatic picture recognizes that these states have the same (0^+) symmetry and that there will thus be an avoided

[a]Department of Chemistry, University of Durham, South Road, Durham DH1 3LE, UK.
[b]Department of Chemistry, Technische Universität Darmstadt, 64287 Darmstadt, Germany.
[c]Department of Physics and Astronomy, University of Alabama, Tuscaloosa, AL 35487.

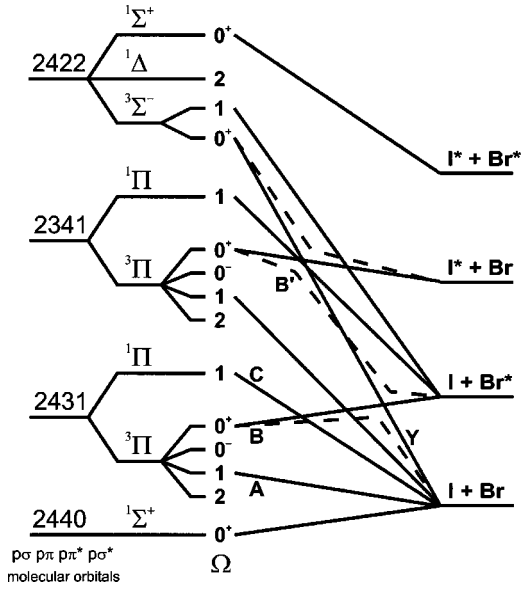

FIG. 1. Diabatic/adiabatic correlation diagram of IBr. The columns on the left hand side represent: the occupancy of the molecular orbitals ($p\sigma p\pi p\pi^* p\sigma^*$) of the individual electronic configurations, the term symbol of the electronic state and the quantum number of the projection of the total angular momentum onto the internuclear axis, Ω. Diabatic and adiabatic correlations are drawn as solid (——) and dashed (– – –) lines, respectively. Only those correlations involving electronic states which can be reached via single photon excitation from the ground state are shown.

crossing in the region of strong configuration mixing. Continued interest in this particular interaction arises from the fact that the coupling between these two states is of ''intermediate strength,'' i.e., the mixing is thus not particularly well described in either a limiting diabatic or adiabatic picture. More recent investigations of the predissociation of these higher v' levels in the *B* state well include experimental and theoretical studies of the resonance Raman spectrum of IBr,[11,12] measurements and analysis of the ''action'' spectrum for forming ground state Br atoms following excitation of jet-cooled IBr molecules in the wavelength range 562–550 nm,[13] femtosecond pump–probe studies of wave packet evolution on the coupled B/Y potentials[14] and two time-dependent wave packet studies of this latter process.[15,16]

The absorption spectrum of IBr is continuous at energies above 18 349 cm^{-1}($\lambda \leqslant 544.84$ nm), the threshold for forming spin-orbit excited Br atoms (henceforth indicated Br*, where the asterisk is intended to distinguish them from ground state products). The absorption maximizes at $\lambda \sim 500$ nm, and thereafter declines monotonically reaching a minimum at ~360 nm.[17] The literature contains many studies of the direct dissociation of IBr molecules following excitation in this region, including two earlier photofragment translational spectroscopy (PTS) studies, at 531 nm[18] and at several different wavelengths in the range 480–530 nm,[19,20] as well as Br* quantum yield measurements at numerous wavelengths in the range 440–540 nm.[21,22] All indicate a substantial population inversion in the Br* and Br products resulting from IBr photolysis at $\lambda \sim 500$ nm. This observation has inspired proposals for a Br* laser, operating on the $^2P_{1/2} \rightarrow {}^2P_{3/2}$ magnetic dipole transition at 2.714 μm, based on 532 nm, or even solar, photolysis of IBr[23,24] and investigations of the adverse effects of I atom quenching of Br*.[25] Two color, time delayed double resonant excitation via the *A* and *B* states of IBr has also been proposed as a test example wherein coherent control (of the Br*/Br product ratio) might be demonstrable in a pulsed experiment.[26] For completeness, we note that the literature also contains reports of at least three PTS studies of IBr photolysis at shorter wavelengths (spanning the range 248–308 nm).[27–29]

Ion imaging methods[30,31] and, particularly, the more recent velocity mapping variant of the technique,[32] are now widely recognized as providing a particularly direct and informative visualization of product branching ratios and the velocity (speed and angular) distribution of fragments arising in photofragmentation processes. Here, as part of an ongoing program devoted to the ''continuum state spectroscopy'' of halogens and interhalogens,[10,33,34] we report the use of such methods in a comprehensive study of the photolysis of jet-cooled IBr molecules over the wavelength range 440–685 nm. Image analysis provides precise threshold energies for the ground, I+Br, and first excited I+Br* dissociation asymptotes, and accurate measures of the electronic branching into these two active product channels and the recoil anisotropy of each set of products, as a function of excitation wavelength. Given such comprehensive experimental data it has proved possible to determine partial cross-sections for parallel (i.e., $\Delta\Omega=0$) and perpendicular (i.e., $\Delta\Omega=\pm 1$) absorptions and, guided by the results of time-dependent wave packet calculations, to deconvolute the separately measured (room temperature) parent absorption spectrum into contributions associated with excitation to the $A\,^3\Pi(1)$, $B\,^3\Pi(0^+)$ and $^1\Pi(1)$ excited states. This analysis of the continuous absorption spectrum of IBr, taken together with the existing spectroscopic data for the bound levels supported by the *X*, *A*, and *B* state potentials,[4,6,7,9] thus allows quantitative determination of the potential energy curves for, and (*R* independent) transition moments to, the *A*, *B* and $^1\Pi(1)$ excited states. For simplicity, and as is the convention for most other halogens and interhalogens, we henceforth assign the label *C* to this $^1\Pi(1)$ state. Further wave packet propagations on the diabatic potentials for the *A*, *B*, and *C* states, allowing for possible transfer of flux between the *B* and $Y(0^+)$ state potentials, and comparison with the experimentally measured, wavelength-dependent product channel branching ratios and recoil anisotropies, provide additional validation of the excited state potentials so derived and allow rather precise determination of the coupling strength between the *B* and *Y* diabatic states. Use of this information in an accompanying investigation—both experimental[13] and theoretical—of the *B/Y* diabatic state coupling and the vibrational level structure of *B* state IBr molecules will form the basis of a separate publication.[35]

II. EXPERIMENT

The experiments were conducted in a new, custom designed and built ion imaging spectrometer. Figure 2 provides a cross-sectional overview of the apparatus, which comprises: (A) a differentially pumped molecular beam source chamber; (B) a separately pumped photolysis chamber,

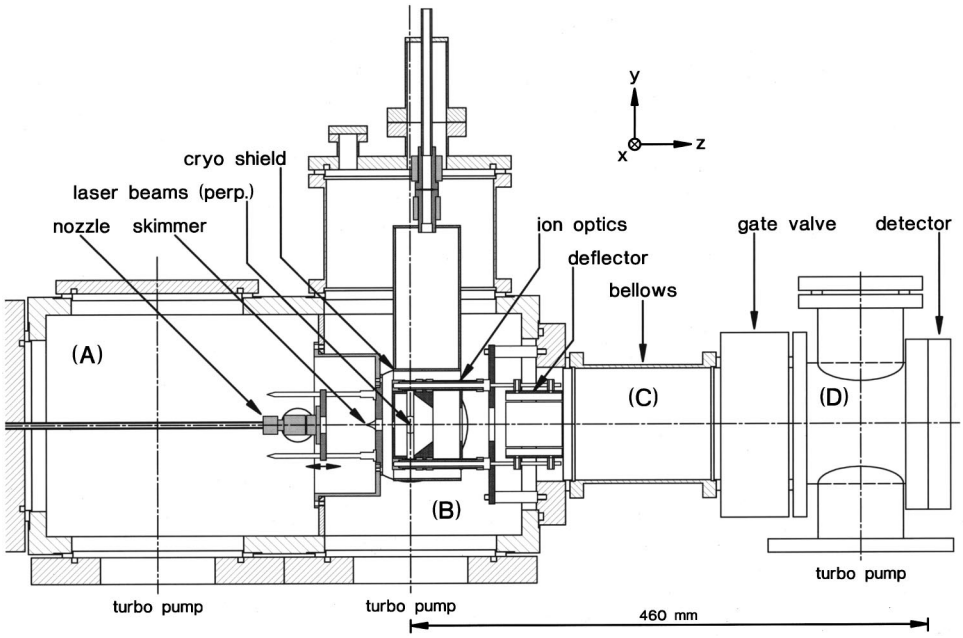

FIG. 2. Vertical cross-section through ion imaging spectrometer comprising: (A) molecular beam source chamber with pulsed nozzle; (B) photolysis chamber with ion optics and liquid nitrogen cooled cryoshield to provide extra pumping of the source region; (c) field free TOF region; (D) detector chamber which can be separated from the remainder by a gate valve. The *x*,*y*,*z* axes are defined as shown (*x*-axis pointing into the plane). This depiction shows the spectrometer with the ''standard'' flight path of $d=460$ mm. This can be reduced to $d=262$ mm by removing the bellows and gate valve or extended, as for the present work, to $d=860$ mm by inserting a nipple between the detector chamber (D) and the detector flange.

equipped with three independently biased, annular electrodes the designs of which have been optimized for velocity mapping, surrounded by a grounded, liquid nitrogen cooled copper cryo-shield to provide additional pumping of the source region; (C) a TOF region; and (D) a separately pumped detector chamber (which can be isolated from the remainder of the experiment by a manually operated gate valve). The coordinate system used in the following description is also shown in Fig. 2.

Chambers (A) and (B) are engineered in the form of a single cuboid (all major flanges ISO-K/F), and separated from each other by an internal bulkhead which supports a centrally mounted skimmer (Beam Dynamics, Model 10.2, 1 mm orifice diameter). The molecular beam is provided by a pulsed valve (General Valve Series 9, 0.5 mm orifice, with Iota One nozzle driver) mounted on 1/4 in. Swagelok tubing, which is user translatable along the *z*-axis and aligned so that the molecular beam passes through the skimmer and along the center axis of the annular ion optic assembly. To minimize degradation of the IBr sample on exposure to stainless steel surfaces, the requisite sample gas mixtures (typically 0.5% IBr in Ar, contained in a Pyrex bulb at a backing pressure of ~760 Torr) is delivered to the main body of the valve through a fine bore PTFE tube located concentrically within the Swagelok piping, and maintained as a slow continuous flow past the rear of the poppet by gentle pumping with a throttled rotary pump. Prior to use, the (solid) IBr sample (BDH) was pumped to remove air and preferentially much of the Br_2 contaminant from the vapor (~4 Torr at room temperature).

The design of the ion optics was guided by numerous simulations using the SIMION 3D software package (Scientific Instruments Services, version 6); the eventual design is illustrated in Fig. 3. The three electrodes (repeller, extractor

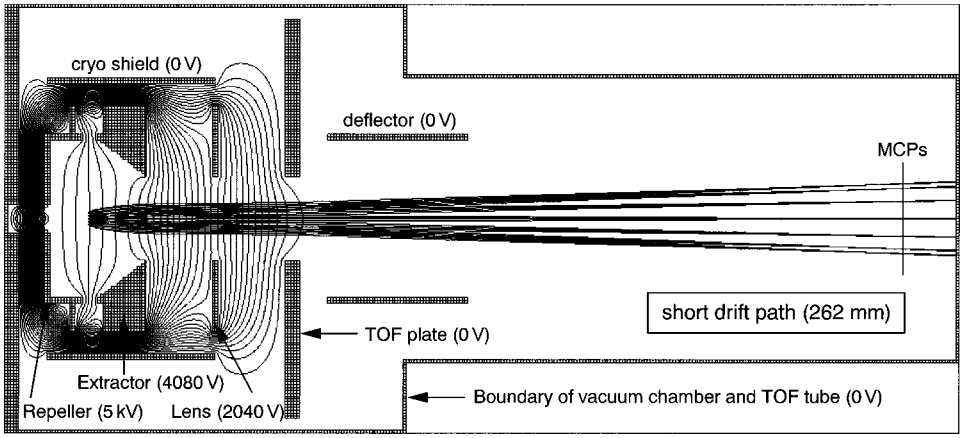

FIG. 3. Detial of ion optic assembly, showing lines of equipotential calculated using SIMION 3D (version 6). The bias voltages shown are those for optimal velocity mapping when using the reduced source–detector flight path of $d=262$ mm by removing the bellows and gate valve. The experiments reported in this study employed $d=860$ mm, for which the experimentally determined optimal electrode voltages were $V_{Rep}=5$ kV, $V_{Extr}=3.95$ kV, $V_{Lens}=2$ kV. Superimposed are ion trajectories originating at different positions in the source volume and with different angles relative to the TOF axis which serve to illustrate the velocity mapping.

and lens) are held rigidly on insulating supports mounted off a single flange, having been prealigned during assembly to ensure maximum parallelism and cylindrical symmetry about the *z*-axis; each is biased by a separate 0–5 kV power supply. The entire ion optic assembly may be demounted as a unit after removal of the stainless steel bellows that constitutes the minimum length TOF tube (C). Spherical and chromatic aberrations can only be minimized, not eliminated, when designing any electrostatic lens.[36] In reaching this eventual design, we paid particular attention to ensuring that all insulating components were screened from any ion in the source region, and that the surrounding cryo-shield induced no field gradients in this region. Figure 3 serves to demonstrate that the field lines in the center of the source region are suitably parallel to one another and perpendicular to the extraction axis, and shows the quality of the velocity mapping in the focal plane of the detector. Our ion trajectory simulations suggest that the present design features reduce chromatic aberration by a factor of ~3.5 relative to that achievable with a ''conventional'' ion optic design, i.e., three optimally separated, biased, parallel, flat annular electrodes, but offer little reduction in the amount of spherical aberration. Figures 2 and 3 show that the spectrometer has been designed with *x* and *y* steering plates at the entrance to the TOF region. These deflector plates were not required in the present work but are included in the design in order (a) to allow the ion cloud to be steered onto the center of the detector (if necessary), or (b), upon application of a suitably timed voltage pulse, to deflect ions of a chosen mass off the detection axis.

The photolysis and probe laser outputs are counterpropagated in the $-x$ and $+x$ directions, respectively, passing between the repeller and extractor electrodes and focused so that their respective foci overlap (in both space and time) with the early time part of each expanding gas pulse. Figure 2 shows the front face of the microchannel plate (MCP) detector 460 mm distant from this source region. For the present work, imaging of relatively heavy, and thus slow moving ions, the image resolution was improved by extending the drift path to 860 mm by insertion of an additional 400 mm stainless steel nipple. The final chamber (D) houses an impedance matched pair of 40 mm diameter active area MCPs mounted in front of a UV enhanced fast phosphor (P47) screen which is viewed by a CCD camera equipped with a time gated image intensifier (Photonic Science).

The three chambers are each pumped by turbomolecular pumps (Leybold Turbovac 151, 145 l/s N_2) backed by two stage rotary pumps (Leybold Trivac D10E). Typical base pressures during operation were 8×10^{-6}–2×10^{-5} Torr in the source chamber, 1×10^{-8} Torr in the photolysis chamber, and 2×10^{-8} Torr in the TOF and detector regions.

Photolysis wavelengths in the range 685–440 nm were provided by a Nd:YAG pumped dye laser (Spectra-Physics GCR-250, operating at 532 nm or 355 nm as appropriate, plus a Sirah Cobra Stretch dye laser); the photolysis laser beam was focused into the interaction volume using a planoconvex quartz lens with $f=20$ cm. This laser output has a specific bandwidth of $\sim0.05\ \mathrm{cm}^{-1}$. As we show below, the photolysis step was easily ''saturated'' particularly near the absorption maximum at $\lambda\sim500$ nm, i.e., a sufficient fraction of the molecules with bonds preferentially aligned parallel to the electric vector, $\boldsymbol{\epsilon}$, of the photolysis pulse could be photodissociated with a single laser shot that the probabilities of dissociation and thus the fragment recoil distributions showed clear deviations from that expected on the basis of projecting the transition moment onto the polarization vector ($|\boldsymbol{\mu}.\boldsymbol{\epsilon}|^2$). Thus typical photolysis pulse energies used were only ~0.6 mJ (at 680 nm), ~0.15 mJ (at 500 nm) and ~0.8 mJ (at 440 nm), in a pulse width of ~7 ns and focused to a diameter in the interaction region of ~0.5 mm (corresponding to a pulse intensity of $\sim10\ \mathrm{MW\,cm^{-2}}$). Ground state I atoms, and both ground and spin-orbit excited Br atoms were ionized, in the interaction region, by two photon resonance enhanced multiphoton ionization (REMPI) via the following transitions:

$$\mathrm{I}(..5p^5;{}^2P^0_{3/2}) \xrightarrow{2h\nu(\lambda=304.67\ \mathrm{nm})} \mathrm{I}(..5p^4 6p^1;{}^2D^0_{5/2}) \xrightarrow{h\nu} \mathrm{I}^+ + e^-, \tag{1}$$

$$\mathrm{Br}(..4p^5;{}^2P^0_{3/2}) \xrightarrow{2h\nu(\lambda=260.62\ \mathrm{nm})} \mathrm{Br}(..4p^4 5p^1;{}^4D^0_{3/2}) \xrightarrow{h\nu} \mathrm{Br}^+ + e^-, \tag{2}$$

$$\mathrm{Br}^*(..4p^5;{}^2P^0_{1/2}) \xrightarrow{2h\nu(\lambda=262.55\ \mathrm{nm})} \mathrm{Br}(..4p^4 5p^1;{}^2S^0_{1/2}) \xrightarrow{h\nu} \mathrm{Br}^+ + e^-, \tag{3}$$

and detected, isotope specifically in the case of atomic Br, by monitoring just those ions impacting on the MCP/phosphor screen with the appropriate TOF. The necessary probe wavelengths were generated by frequency doubling (in KDP or BBO, as appropriate) the output of an excimer pumped dye laser (Lambda-Physik Compex 201 plus FL2002 operating with the dyes Kiton Red and Coumarin 503, respectively). Images were obtained by repeatedly scanning backward and forward across the Doppler profile of the fragment transition of interest. For all definitive experiments reported here, both the photolysis and probe laser photons were polarized vertically in the laboratory frame, i.e., with their respective $\boldsymbol{\epsilon}$ vectors along *y*, but, as discussed more fully below, checks were made to establish that the measured images were insensitive to the choice of probe transition and/or to the direction of $\boldsymbol{\epsilon}_{\mathrm{probe}}$.

Each ion image resulting from a single laser shot is processed with a centroiding algorithm provided with the commercial camera software DaVis (La Vision) running on a Pentium II 350 MHz PC. This algorithm takes advantage of the finite size of an individual ion impact as it is seen by the camera (typically 2–3 pixel FWHM) by analyzing 3×3 pixels around its maximum to calculate the center of gravity for this particular event. The intensity of this event is added at the appropriate (x,y) pixel coordinate to a buffer, and the complete image is obtained by accumulating such counts over 10 000–20 000 laser shots. The signal levels (i.e., events per laser shot) for each of the measurements were carefully

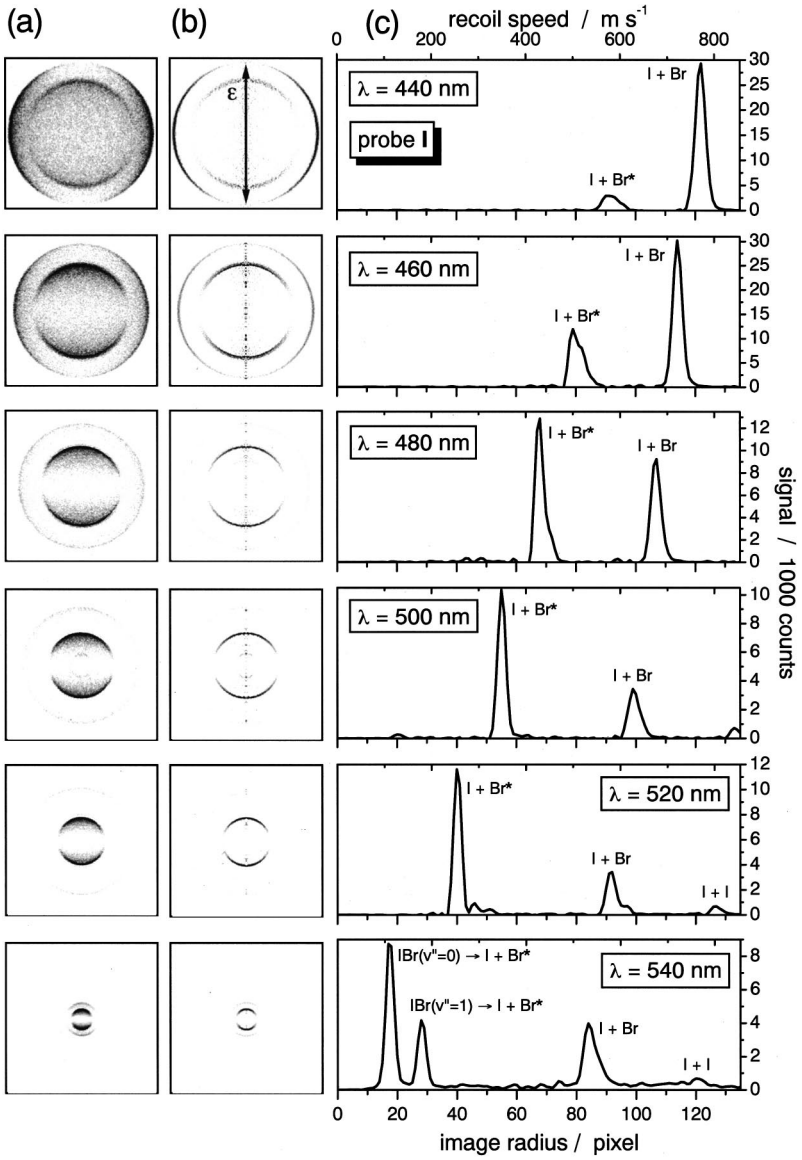

FIG. 4. (a) Unprocessed raw ion images and (b) 2D slices through the reconstructed 3D recoil distributions of ground state I atoms resulting from photolysis of jet-cooled IBr molecules at six wavelengths in the range 440–540 nm. Only the 251×251 pixels center parts of the images are shown. ϵ denotes the electric vector of the photolysis light (i.e., axis of cylindrical symmetry). (c) shows the corresponding velocity distributions, with features due to the I+Br and I+Br* product channels (and the I+I products from photolysis of I_2 contaminant) indicated.

chosen in order not to ''saturate'' the algorithm by multiple impacts onto the same detector position within a single laser shot and in order not to blur the image due to space charge effects. Typically, pulse energies of 2–10 μJ of probe light ($\sim$20 ns pulse duration, focused to a beam diameter of $\sim$0.015 mm using an $f=13$ cm plano-convex quartz lens, corresponding to pulse intensities $\sim$250 MW cm^{-2}) were used to ensure that the required small signal levels were below $\sim$50 ions per shot.

Further analysis requires the reconstruction of the 3D velocity distributions from the accumulated 2D ion images for which purpose an algorithm based on the filtered back-projection proposed by Sato *et al.*[37] is applied. Prior to reconstruction, the images were processed in the following manner: (1) In order to reduce the noise in the raw ion images, which is unavoidable with the present centroiding algorithm and which will be amplified by the reconstruction procedure, the images were smoothed using a 2D Gaussian filter (with a FWHM of 2 pixels). (2) It is important to define the center of the images, i.e., the position of the velocity origins, as precisely as possible. This was achieved with an automatic procedure which uses the underlying symmetry of the photodissociation process in comparing, respectively, the upper/lower and left/right halves of each image with respect to a test origin, and minimizes the squared differences with sub-pixel resolution. The centering was tested by performing the reconstruction on each quadrant individually and comparing the resulting velocity distributions, which turned out to be almost identical and only showed minor differences in the intensities. (3) Finally, the images were four-fold symmetrized (in order to increase the signal-to-noise ratio) and (4) the 3D velocity distributions reconstructed, from which the velocity and angular distributions were extracted. To determine meaningful errors, the total signal of each image (i.e., the number of ion events) is conserved, and the statistical errors (proportional to the square root of the number of counts in an individual pixel) are propagated throughout the whole reconstruction and analysis process.

The quality of ion images recorded with this new ion imaging spectrometer is very high [see column (a) of Fig. 4 and images presented in Ref. 10]. The images show very little asymmetry, and sharp structures observed at the longer

wavelengths are attributable to photolysis of parent molecules with different levels of vibrational excitation. The ground state spectroscopy[9] and the bond dissociation energy[10] are both well established. Thus the velocity (in pixel space) of products arising from monochromatic photolysis of parent molecules in any given rovibrational level can be calculated. The observed velocity distributions are the result of dissociations originating from a range of parent quantum states. These can be simulated as a sum of Gaussian profiles, each centered at the velocity (pixel) position appropriate for the originating parent level of interest, with relative weightings appropriate for a Boltzmann parent rotational state population distribution. This rotational temperature, the relative intensities attributed to the various parent vibrational levels, the width of the Gaussian profiles, and the pixel to velocity scaling factor are all adjustable parameters in the fit. The results reported previously[10] establishing $T_{\mathrm{rot}}=12\pm1$ K, while the relative intensities of the vibrational levels could best be simulated (by calculating the appropriate free←bound Franck–Condon overlaps) assuming a vibrational temperature, $T_{\mathrm{vib}}=250\pm10$ K.

III. RESULTS AND DISCUSSION

A. Br* product branching fraction, Γ

Figure 4 displays raw images (left hand column) and 2D slices through reconstructed 3D recoil distributions (center column) of ground state I atoms resulting from photolysis of jet-cooled IBr molecules at six different wavelengths in the range 440–540 nm. Each was recorded using the 860 mm flight path, with the same voltage settings on the ion optics ($V_{\mathrm{Rep}}=+5$ kV; $V_{\mathrm{Extr}}=+3.9$ kV; $V_{\mathrm{Lens}}=+2$ kV) and with the ϵ vector of the photolysis radiation aligned vertically, as indicated. The corresponding velocity distributions are shown on the right of each image. IBr exists in equilibrium with I_2 and Br_2. Since I_2 absorbs, at all photolysis wavelengths relevant to Fig. 4, images obtained by monitoring ground state I atom products will necessarily exhibit additional (generally weak) rings associated with formation of two ground state I atoms (or an I+I* combination) from I_2 photolysis. Such features are indicated in Fig. 4. They present no problem in the image analysis that follows, since energy conservation dictates that they appear at velocities (and thus radii) well separated from the I+Br/Br* products of interest. The fact that the parent sample contains $I^{79}Br$ and $I^{81}Br$ molecules, in roughly equal abundance, affects the velocity resolution of the I atoms from IBr photolysis, however. Because of the mass dependence of the momentum partitioning upon fragmentation, I atoms formed in association with a ^{79}Br atom will recoil 0.8% slower than those deriving from $I^{81}Br$ photolysis (for the same total kinetic energy release). This splitting is not resolved even in the present high resolution images, since it corresponds to less than one pixel in image radius, though it is worth recalling that we could distinguish this velocity difference when monitoring the individual Br isotopes arising in the near threshold dissociation of IBr via the shift in the peak positions in the respective velocity profiles (each of which can be fitted with sub-pixel resolution).[10] All modeling of images recorded on the I atom product thus assumed the partner fragment to be a hypothetical ^{80}Br species.

Even a cursory inspection of these images suffices to illustrate that both the branching into ground and spin-orbit excited state Br atoms, and the recoil anisotropy of the I+Br products, show a marked wavelength dependence. Before analyzing these dependencies in detail, however, it is necessary to review possible factors that can affect the detailed appearance of such ion images. One is saturation. As mentioned earlier, signal levels were maintained at or below ~50 ion impacts per laser shot in order to minimize the chances of multiple impacts on the same detector position, and any image blurring from space charge effects. Many different combinations of molecular beam seeding ratio and density, and photolysis and probe laser intensities, can yield such low signal levels, but not all will necessarily be free of (other) ''saturation'' effects. In particular, in the present experiments, the measured angular distributions of the recoiling products were found to be markedly dependent on the photolysis laser pulse energy. This was particularly evident for signal appearing at $\theta\sim0°$ (where θ is the angle between the ϵ vector of the photolysis laser radiation and the direction of photofragment recoil); only at very low incident pulse energies (below ~150 μJ pulse^{-1} for $\lambda\sim500$ nm, near the peak of the parent absorption) was the angular distribution of the I+Br* products unarguably independent of the incident photolysis pulse energy. Possible artifacts, such as this saturation of the photolysis transition, become strikingly obvious in high resolution, high signal to noise images.

Halogens and interhalogens are proving popular test molecules for demonstrating (and interpreting) the alignment and/or orientation of atomic products arising in photodissociation processes.[38–42] The primary concern of the present work is to provide accurate measures of the branching ratios and angular anisotropies of the product channels active in the visible photodissociation of IBr but, since the latter at least can be sensitive to such orientation and alignment effects, it was necessary to test for their presence. Any substantial product alignment will reveal itself as an apparent $P_4(\cos\theta)$ moment in the angular anisotropy of the image and/or via differences in the detailed appearance of the image when recorded with the probe polarization aligned normally (i.e., along y) or parallel to the TOF axis (along z). To test for these effects we recorded I atom images from IBr photolysis at 499.9 nm, using these two orthogonal polarizations and two different I atom probe wavelengths—at 304.67 nm [Eq. (1)], and at 307.74 nm, using the $^4S^0_{3/2}\leftarrow\leftarrow{}^2P^0_{3/2}$ two photon transition.[43] The angular anisotropies displayed by the various images were indistinguishable by eye and the β parameters extracted (see below) were the same within their corresponding error bars, encouraging the view that any product alignment effects are sufficiently small to have negligible influence on the branching ratios and angular anisotropies reported in this work. Any orbital alignment of the I atom photofragments will degrade (to ~23% of the nascent value) through coupling with the I=5/2 nuclear spin, on a time scale that is short compared to the laser pulse duration. Given this extent of hyperfine depolarization, we can actu-

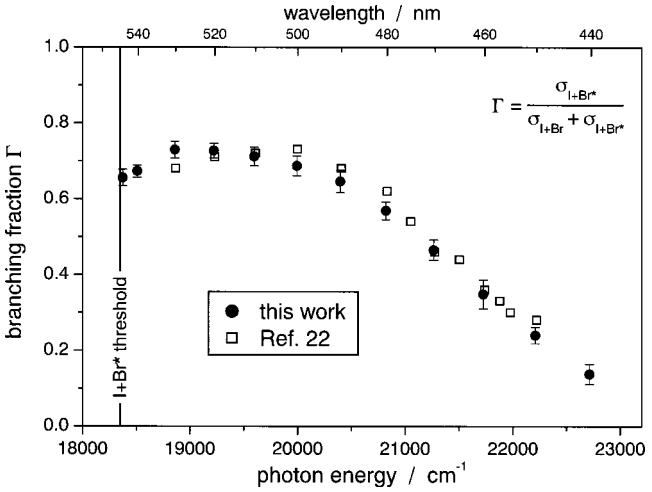

FIG. 5. Br* photofragment branching fractions, Γ, resulting from photolysis of jet-cooled IBr molecules measured in the present work (●), plotted as a function of excitation wavelength. The error bars represent the $\pm 1\sigma$ statistical error band of the measurements. Also shown are the previous branching fraction measurements of Leone and co-workers (□, Ref. 22).

ally quantify the total laboratory frame alignment, $A_0^{(2)}$, in the case of the former probe transition, for which line strength factors are known[41] by analysis of images recorded with different laser polarizations. Use of Eq. (31) of Ref. 41 yields a value $A_0^{(2)} \sim 0.08$ (corrected for hyperfine effects), far from the limiting values of $+4/5$ and $-2/5$ associated with a fully aligned sample (in the high J limit). Further support for the view that there is minimal alignment of the atomic products formed at all photolysis wavelengths investigated in this work is provided by the facts that: (i) none of the fits to the measured angular distributions is improved significantly by inclusion of a $P_4(\cos\theta)$ term; and (ii) in photolyses where both I and Br (or Br*) fragments have been imaged, the derived recoil anisotropies are identical.

Figure 5 shows a plot of the wavelength dependent branching fraction,

$$\Gamma = \frac{\sigma_{I+Br^*}}{\sigma_{I+Br^*} + \sigma_{I+Br}} \tag{4}$$

(where σ_{I+Br^*} and σ_{I+Br} are the relative cross-sections for the respective product channels), deduced from analysis of I atom images recorded in this work, together with the results of the earlier room temperature, time-resolved laser gain versus absorption measurements of Leone and co-workers.[22] The excellent agreement is gratifying. The results demonstrate clearly that the spin-orbit excited I+Br* fragmentation channel is open at the thermodynamic threshold ($D_0 = 18\,349$ cm^{-1},[10] corresponding to $\lambda_{phot} \leqslant 544.84$ nm), that Γ peaks at a value of ~0.75 at $\lambda_{phot} \sim 525$ nm, and that IBr photolysis at all wavelengths in the range $544 > \lambda > 475$ nm leads to an inverted spin-orbit population distribution in the Br atom products.

B. Product angular anisotropies

Panel (a) in Fig. 6 shows the experimentally measured I atom product velocity distribution resulting from IBr photolysis at 520 nm in greater detail, together with a plot [panel (b)] illustrating the deduced variation in recoil anisotropy parameter, β, with fragment recoil velocity. The β values are derived by analyzing the reconstructed images, as a function of radius, r (and thus recoil velocity, v), in terms of the function

$$I(v,\theta) = f(v)\{1 + \beta P_2(\cos\theta)\}, \tag{5}$$

where θ is the angle between the ϵ vector of the photolysis laser radiation and the direction of photofragment recoil, $f(v)$ is the speed distribution of the detected photofragment, β is the anisotropy parameter, and $P_2(x) = (3x^2 - 1)/2$ is a second order Legendre polynomial.[44] β takes limiting values of $+2$ and -1 in the case of prompt dissociations following, respectively, a pure parallel (i.e., $\Delta\Omega = 0$) or pure perpendicular (i.e., $\Delta\Omega = \pm 1$) excitation of the parent diatomic molecule. Panels (c)–(f) show representative angular distributions, each of which has been normalized to unit area, for different r (and thus v), together with the respective best-fit curves. Clearly, the slowest feature ($r \sim 40$), associated with formation of I+Br* products is well described by $\beta = 2$, implying that these products arise as a result of prompt dissociation following excitation via an (essentially) pure parallel transition. The fastest feature, at $r \sim 127$, is due to I atoms formed in the dissociation of I_2. The angular distribution of these products fits well to $\beta \sim -1$, indicating that the formation of ground state I atoms from I_2 photodissociation at 520 nm results from a perpendicular parent excitation. Note that the large error bars in panels (e) and (f) arise from the low signal levels, and thus the poor signal-to-noise ratios, associated with these features.

Of greater interest in the context of the present work is the recoil anisotropy of the I atoms formed in association with ground state Br products, for which the best-fit β evolves from positive to negative values with increasing r, and thus recoil velocity. Similar trends were observed for the I+Br products formed at all excitation wavelengths in the range 490–540 nm. Since the photolysis is performed using a narrow bandwidth laser source, and the products are both atoms, the faster I+Br product recoil velocities must derive from more internally excited parent molecules. Our previous simulations[10] of images of the Br products arising in the near threshold dissociation of IBr established a parent beam rotational temperature of $T_{rot} \sim 12$ K. A rotational temperature of 12 K corresponds to an average rotational energy of ~8 cm^{-1} which, if released as kinetic energy would amount to less than one pixel at these recoil velocities ($r \sim 91$). Thus we conclude that the fastest I atoms must arise from excitation (and dissociation) of vibrationally excited parent molecules [the vibrational level spacing in IBr(X) is 267 cm^{-1}]. In order to explain the observed velocity dependent β parameter for the I+Br products we would then require that 520 nm excitation promotes ground and vibrationally excited IBr molecules to dissociative excited state potentials with $\Omega' = 0$ and 1 with very different relative efficiencies. Further indication that such may indeed be the case is provided by the observation that *all* I+Br products resulting from IBr photolysis at yet shorter excitation wavelengths ($\lambda_{phot} < 490$ nm) exhibit an angular anisotropy parameter $\beta \ll 2$. We re-

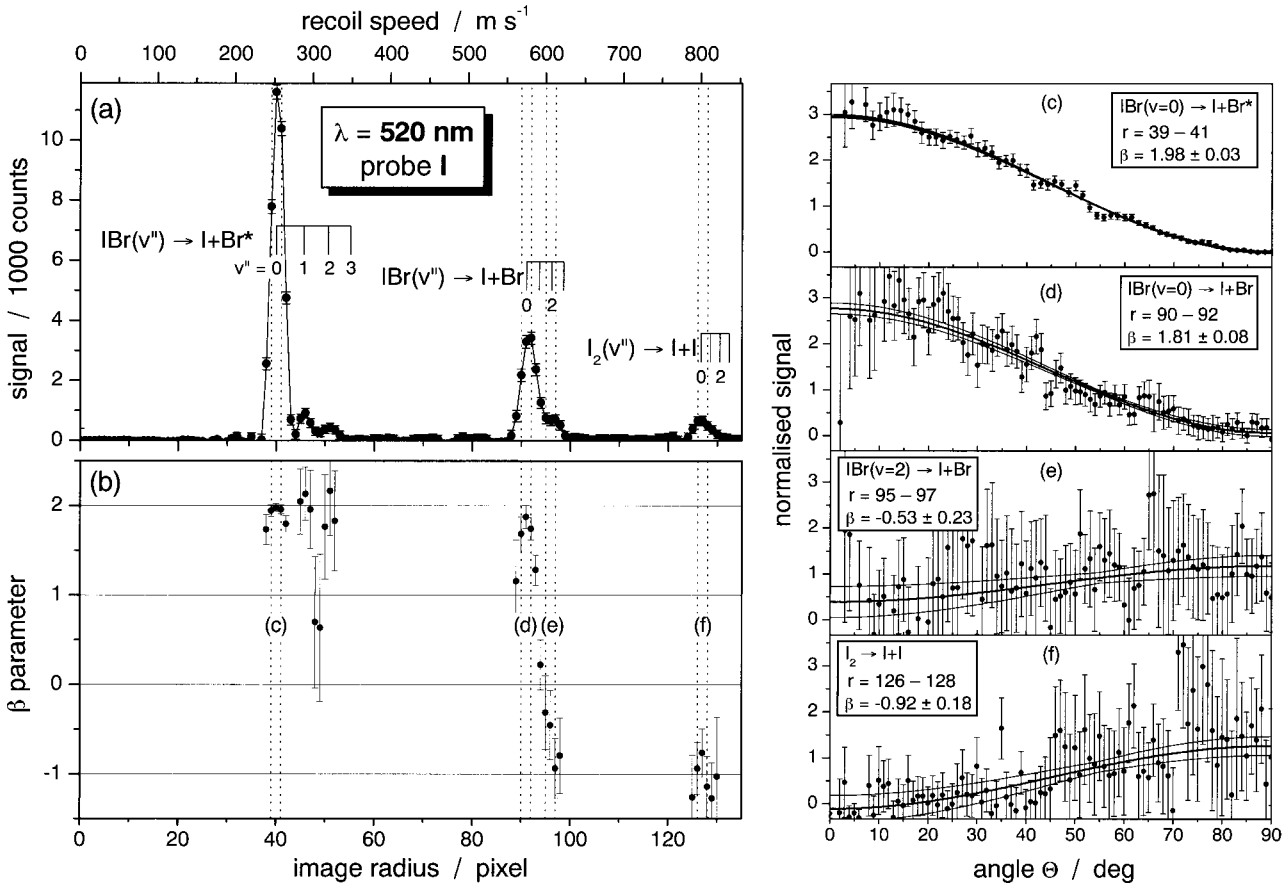

FIG. 6. (a) Velocity distribution of I atoms resulting from 520 nm photolysis of jet-cooled IBr molecules, and the accompanying I_2 impurity, together with (b) a plot showing the variation of the recoil anisotropy parameter, β, with recoil velocity. All error bars represent the $\pm 1\sigma$ (statistical) error bands of the measurements. The right hand panels (c)–(f) display the variations in the angular distributions of different velocity sub-groups (i.e., different image radii r) within the total I atom yield. All four distributions are normalized to unit area. The best-fits according to Eq. (5) (solid lines) are shown together with their $\pm 1\sigma$ error bands (dashed lines). Note that the large error bars, particularly in panels (e) and (f), reflect the poor signal-to-noise ratio in the corresponding parts of the image.

turn to these observations later, after derivation of the best IBr excited state potential functions yet available.

Figure 7 shows reconstructed 3D recoil distributions of the ^{79}Br atom fragments arising in the photolysis of jet-cooled IBr molecules at 630 nm and at 520 nm, and of the ^{79}Br* fragments that result from near threshold photodissociation at 540 nm. Again, the ϵ vector of the photolysis radiation was vertical, as indicated, but the radii of the various rings in the different images are not directly comparable with one another because not all were taken using the same extraction voltages. Plots showing the corresponding velocity dependent intensity and recoil anisotropy distributions are displayed to the right of each image. These are arguably the best images on which to base any discussion of the image resolution achieved to date, though it should be fairly obvious that IBr (with its very closely spaced rovibrational level structure) is a far from ideal test-case molecule with which to demonstrate the ultimate experimental resolution. The sharpest ^{79}Br images were fitted assuming that products arising from a parent rovibrational quantum state spanned 3.7 pixels (FWHM) after application of the 2×2 pixel Gaussian filter [or 3.2 pixels (FWHM) with no filter function]. This translates to a velocity spread of 30 m s^{-1} (26 m s^{-1} without filter function), of which only a small fraction can be attributed to the spread of parent velocities perpendicular to the molecular beam axis and the pixel ''resolution'' (including Gaussian filter) of the camera. The remainder is presumably attributable to residual imperfections in the ion optics or, more probably, to small image distortions caused by the optical coupling of the phosphor screen to the camera and/or to imperfect synchronization between the camera and frame grabber. For comparison with other ion imaging systems, the 30 m s^{-1} velocity resolution presently achieved translates into an energy resolution, $\Delta E/E$, $\sim$3.8% for a Br atom recoiling with a kinetic energy of 1 eV.

The Br image recorded at $\lambda_{phot}=630$ nm is representative of all images taken in the wavelength range $685\geqslant\lambda_{phot}\geqslant 630$ nm, each of which shows the I+Br product recoil anisotropy to be well described in terms of Eq. (5) with $\beta=-1$ in agreement with the well-established perpendicular nature of the $A(1)\leftarrow X(0^+)$ transition. Imaging studies in the 545–600 nm region, where the jet-cooled parent absorption spectrum comprises a progression of resonances associated with B-X vibronic transitions superimposed on an underlying continuum and β is a fluctuating function of wavelength, will be reported separately.[35] The Br* image recorded at $\lambda_{phot}=540$ nm is characteristic of all other Br* images taken in the range $540\geqslant\lambda_{phot}\geqslant 440$ nm, and is well

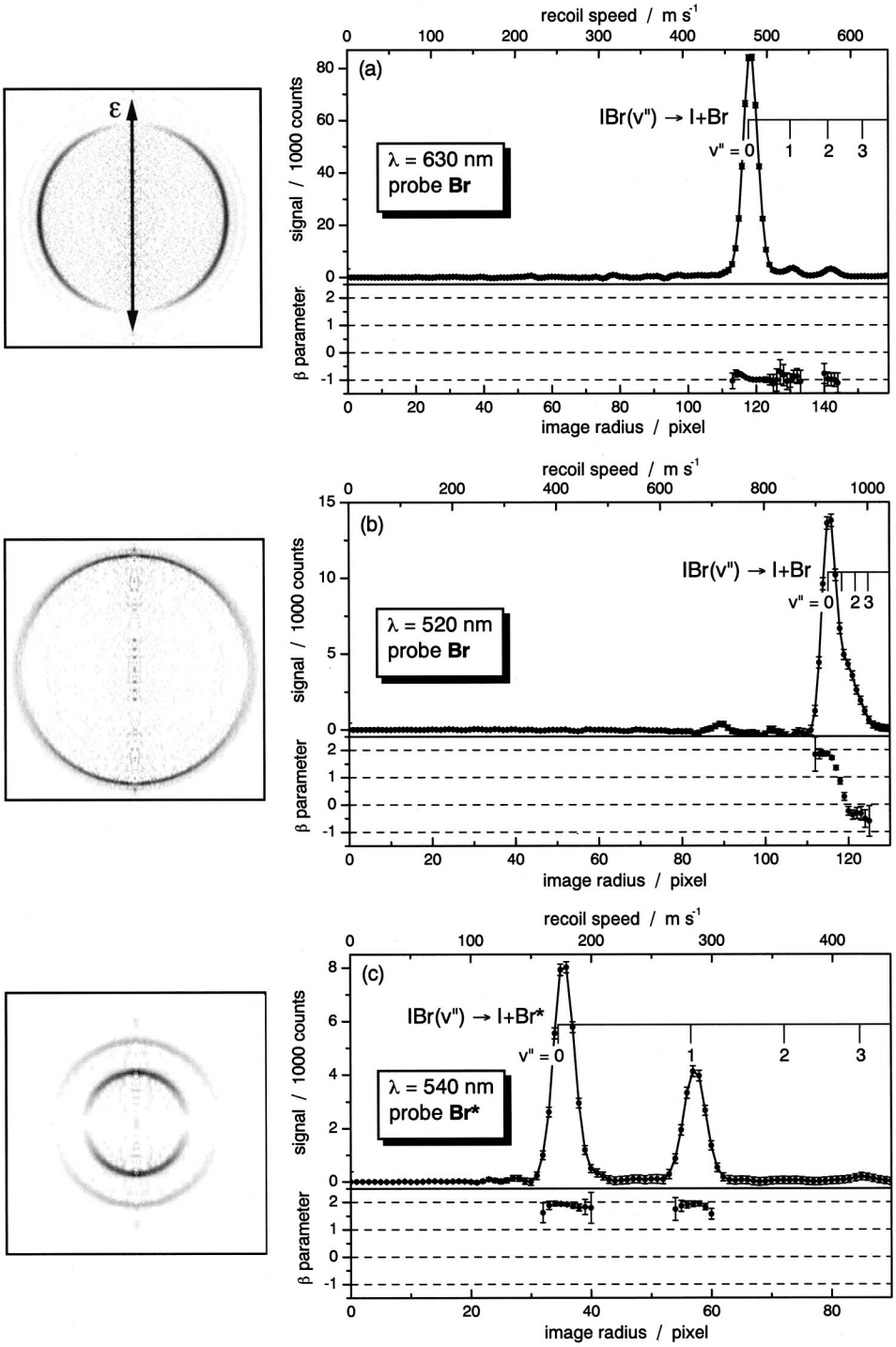

FIG. 7. The left hand panels show 2D slices through the reconstructed 3D recoil distributions of ground state ^{79}Br atoms resulting from photolysis of jet-cooled IBr molecules at (a) 630 nm and (b) 520 nm, and of (c) ^{79}Br* atoms from IBr photolysis at 540 nm. Reduced ion optic voltages were used when recording (a): $V_{Rep}=1.25$ kV, $V_{Extr}=1.0$ kV, $V_{Lens}=0.5$ kV, and (c) $V_{Rep}=1.9$ kV, $V_{Extr}=1.5$ kV, $V_{Lens}=0.75$ kV. Again, only the center part of each image, corresponding to the indicated velocity/pixel interval, is displayed. ϵ denotes the electric vector of the photolysis light. The right hand panels show how the corresponding product yield and recoil anisotropies vary with the recoil velocity.

described by $\beta\sim 2$. Only at wavelengths closer to the energetic threshold ($\lambda_{phot}=544.84$ nm) do the Br* images show any clear deviation from limiting behavior. Careful analysis of the I+Br* ring in these images recorded at photon energies just above the dissociation threshold shows β declining with increasing pixel radius. Such trends are wholly consistent with a progressive breakdown of the axial recoil approximation with increasing parent rotational, and with the associated dramatic behavior observed at energies just above the I+Br dissociation threshold.[10,45]

The image of the ground state Br atoms measured following IBr photolysis at $\lambda_{phot}=520$ nm shown in Fig. 7(b) merits more comment. These Br atoms partner the I atoms that give rise to the middle peak in the velocity distribution shown in Fig. 6. The deduced velocity dependence of the recoil anisotropy parameter of these Br products is in excellent accord with that found for the partner I atoms (Fig. 6). This is an important observation. The images in Fig. 7 have higher velocity resolution than the I images, in part because they are isotope specific (TOF separation allows monitoring of just the ^{79}Br atom product) and also because they were deliberately recorded with lower ion optic voltages (in order to expand the image on the detector). The quantitative agreement between the β versus velocity plots obtained by mea-

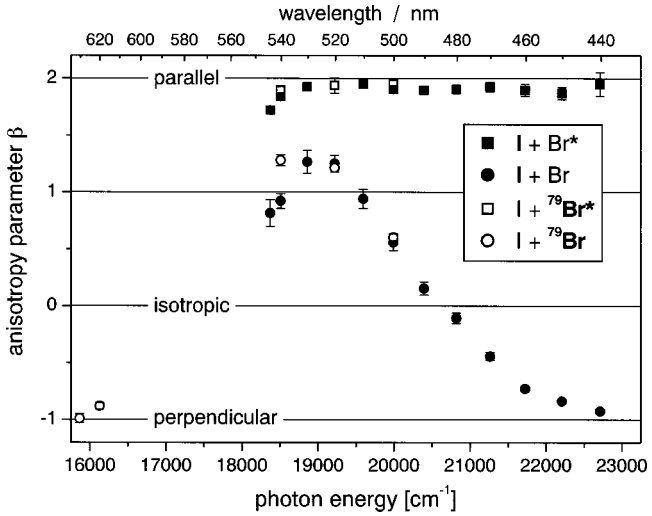

FIG. 8. Plot showing the wavelength dependence of the angular anisotropy parameters for the I+Br and I+Br* product channels as determined by analysis of images obtained by monitoring the I (filled symbols) and ^{79}Br (open symbols) products. The β parameter for a given spin-orbit product channel is obtained by identifying the radius r of the maximum signal associated with that channel, and fitting the angular distribution of all signal in the spread of radii in the vicinity of r that contain >10% of the peak signal. The error bars represent the $\pm 1\sigma$ error bands of the measurements.

suring the I (Fig. 6) and ^{79}Br [Fig. 7(b)] atoms and the fact that, as Fig. 6 showed, the other product channels (I+Br*, and I+I from the I_2 impurity) imaged at this photolysis wavelength show constant, limiting β values across the whole peak profile, serves to reinforce the conclusion that the observed velocity dependent β is a genuine photophysical effect requiring explanation and not, for example, some artifact of the design or operation of the ion optics.

Figure 8 presents a compilation of all of the angular anisotropy measurements recorded in the present work. Clearly, given the foregoing discussion of the velocity dependence of the β parameter for the I+Br products arising in IBr photolysis at $\lambda_{phot} \sim 520$ nm, we need a protocol for ascribing a single β value to the flux associated with any given product channel. For the purpose of this plot, we identify the radius r of the maximum signal associated with any given product channel of interest in the velocity distribution, and fit the angular distribution of all signal in the spread of radii in the vicinity of r that contain >10% of the peak signal. The present findings are in good qualitative agreement with the one previous estimate of β for the I+Br and I+Br* products from IBr photolysis at 490 nm,[20] and demonstrate that the measured anisotropy of the ground state product channel is sensitive both to the parent excitation wavelength and, as Fig. 6 showed, the extent of parent internal (vibrational) excitation.

C. Total and partial absorption cross-sections

The B state is the only excited state of 0^+ symmetry, i.e., that can be reached via a $\Delta\Omega = 0$ vertical transition from the ground state, in the energy range of current interest (compare Fig. 1). In a diabatic picture, the B state correlates with I+Br* products, but both the documented predissociation of B state levels with $v' \geqslant 3$[7,13] (i.e., at energies well below this excited asymptote) and the present observation of a substantial parallel contribution (i.e., $\beta > 0$) to the I+Br products formed above this asymptote indicate that parallel absorption can lead to formation of ground state products. The latter reflects the role of the well documented interaction of the diabatic B and Y potentials at extended bond lengths, and encourages analysis of the present data to estimate a wavelength dependent partial cross-section for parallel absorption. Since the wavelength dependence of the branching fraction, Γ (Fig. 5), and the β parameters for the individual product channels leading to ground and spin-orbit excited bromine atoms (β_{Br} and β_{Br*}, respectively, see Fig. 8) are known, we can calculate an effective anisotropy parameter, β_{eff}, for the total product flux at any given wavelength from the expression

$$\beta_{eff} = \Gamma \beta_{Br*} + (1-\Gamma)\beta_{Br}. \tag{6}$$

Integrating each image over all r and then fitting the result in terms of Eq. (5) should yield the same β_{eff} values, but the former procedure is preferred since it is less susceptible to the inevitable background noise between real features in the image. Given $\beta_{eff}(\lambda)$, the wavelength dependent probabilities for parallel and perpendicular absorption, $P_{par}(\lambda)$ and $P_{perp}(\lambda)$, follow from

$$P_{par} = (\beta_{eff} + 1)/3 \tag{7a}$$

and

$$P_{perp} = (2-\beta_{eff})/3 = (1-P_{par}). \tag{7b}$$

The simple summation in Eq. (6) is valid since, as shown by Siebbeles *et al.*,[46] the effective anisotropy parameter is separable into contributions from individual excitations even in the case of coherent excitation of overlapping parallel and perpendicular absorptions (such as have been invoked to explain polarization of the angular momentum of atomic photofragments[42]).

P_{par} and P_{perp} can be converted to σ_{par} and σ_{perp}, the partial cross-sections for parallel (i.e., $B-X$) and perpendicular absorption, if the total absorption cross-section is known. Unfortunately, the absorption spectrum of IBr vapor reported by Seery and Britton[17] only spans the wavelength range $600 \geqslant \lambda \geqslant 220$ nm, and thus omits much of the $A-X$ absorption system in the red. We therefore re-recorded the entire UV/visible spectrum of five different IBr samples (each with its own particular but inevitable Br_2 and I_2 contamination), and of pure Br_2 and I_2, across the range $800 \geqslant \lambda \geqslant 250$ nm, at 2 nm resolution, using a Perkin Elmer Lambda Bio 10 spectrometer. All samples were pumped at room temperature to remove air and, in the case of IBr, to remove preferentially much of the Br_2 contaminant. Figure 9 shows a representative spectrum, in which structured absorption arising from residual I_2 is clearly visible. This latter absorption can be removed by subtraction of an appropriately weighted absorption spectrum of pure I_2. Br_2 contributions (if present at all) can similarly be removed, after comparison of spectra recorded with different IBr samples. All five ''pure'' IBr spectra obtained after subtraction of appropriate Br_2 and I_2 contributions from the measured absorption

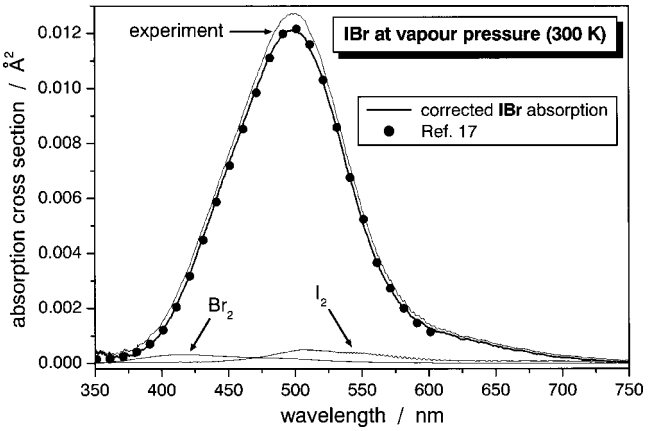

FIG. 9. Room temperature absorption spectrum of an IBr sample over the wavelength range $750 \geqslant \lambda \geqslant 350$ nm, together with suitably scaled spectra of pure I_2 and Br_2. The bold solid curve attributable to pure IBr absorption was obtained by subtraction of these latter two absorption profiles (see text) and was then vertically scaled to match the absolute values from Ref. 17 shown as points (●). The latter have been red shifted by 1.3 nm to give best overlap with the present measurements.

spectra were essentially identical. Figure 9 shows the final pure IBr absorption spectrum throughout the $750 \geqslant \lambda \geqslant 350$ nm range of current interest. Where comparison is possible, the deduced absorption profile is in good agreement with those reported previously by Seery and Britton,[17] and by Haugen *et al.*,[22] though careful simulation of the vibronic structure evident in the I_2 spectrum allows precise calibration of the wavelength scale in Fig. 9 and indicates that the wavelengths reported in the former work all need to be red-shifted by 1.3 nm. Because the absolute pressure of the gas samples used in recording these spectra could not be controlled precisely, we take the literature absorption cross-sections[17] to define the vertical scale in Fig. 9.

Figure 10 shows the deduced absorption profile of pure IBr together with the experimentally determined σ_{par} and σ_{perp} partial cross-sections (as symbols ● and □, respectively), obtained by scaling the total absorption at any given wavelength by the relevant P_{par} and P_{perp} values.

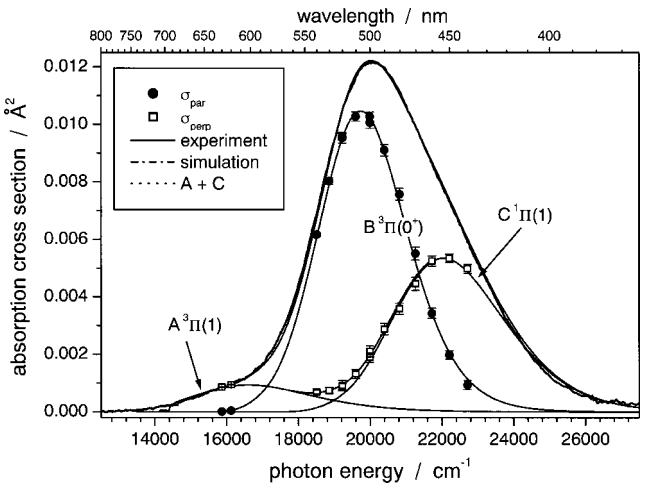

FIG. 10. Optimum deconvolution of the total room temperature absorption spectrum of IBr (bold curve) into $\sigma_{A-X}(\nu)$, $\sigma_{B-X}(\nu)$ and $\sigma_{C-X}(\nu)$ partial cross-sections using the potentials shown in Fig. 11 and parameterized in Table I. The symbols (● and □) show, respectively, the experimentally derived cross-sections for parallel, σ_{par}, and perpendicular absorption, σ_{perp}, derived using Eq. (7). The ''steps'' in the σ_{A-X} curve at $\sim 14\,500$ cm^{-1} correspond to the dissociation limits for IBr $(v''=0,1,\ldots) \rightarrow \text{I}+\text{Br}$ and are an artifact of the output of the wave packet calculation.

D. Determination of potential energy functions for the $A\,^3\Pi(1)$, $B\,^3\Pi(0^+)$, and $C\,^1\Pi(1)$ states

We now seek to construct potentials compatible with the available partial and total absorption cross-section data. The ground state potential has been parametrized previously, most recently by Nelander *et al.*[9] using a modified Morse function of the form:

$$V_X(z) = D_e \left[\frac{1-e^{-\beta(z)}}{1-e^{-\beta(\infty)}} \right]^2 + T_e , \tag{8}$$

with

$$z = \frac{R-R_e}{R+R_e}, \quad \beta(z) = z \sum_{i=0}^{n} \beta_i z^i ,$$

and

$$\beta(\infty) = \sum_{i=0}^{n} \beta_i .$$

Values for the β_i coefficients $(i \leqslant 4)$, the equilibrium bond length, R_e, and D_e were taken from Table 6 of Ref. 9. Unfortunately, the D_e value of $14\,660$ cm^{-1} listed therein is 138 cm^{-1} less than our recent precise determination of the ground state well-depth $D_e = 14\,798$ cm^{-1}.[10] Given the partial absorption cross-sections this discrepancy would shift the deduced repulsive walls (see below) of the corresponding excited state potentials significantly to higher energies. Thus, in order to reproduce both the vibrational term values given by the Dunham coefficients of Ref. 9 and the dissociation limits of the excited state potentials, the entire ground state potential was shifted down in energy by setting $T_e = -138$ cm^{-1} in Eq. (8). This ground state potential defined by Eq. (8) and the parameters listed in Table I allows calculation of the wave functions for the thermally populated ground state levels $(v'' \leqslant 3)$ used when calculating the partial and total absorption spectra (below). The ground state potential is otherwise irrelevant for the calculation of the excited state dynamics, so the small change in D_e implied by this manipulation has no affect on the results of the wave packet calculations presented in Sec. III E.

Guided by the deduced partial cross-section determinations we can anticipate that the long wavelength shoulder to the absorption spectrum arises from the $A-X$ (perpendicular) absorption, that the $B-X$ parallel transition is the dominant contributor at the absorption maximum and that the perpendicular component evident at higher energies will be attributable to the $C-X$ transition. The total absorption spectrum in the wavelength range of interest will thus be sensitive to the repulsive walls of all three excited state potentials. These potential functions were determined iteratively. In each case, a suitable function was fitted to RKR turning points for the bound part of the potential, when appropriate (see below), and to additional points in the Franck–Condon region, ini-

TABLE I. Parametrization of diabatic potentials for the $A\,^3\Pi(1)$, $B\,^3\Pi(0^+)$, $C\,^1\Pi(1)$, and $Y(0^+)$ states of IBr. The individual parameters are defined by the corresponding equations. μ denotes the R independent transition moments of the corresponding transitions from the X state deduced from deconvolution of the absorption spectrum with an estimated uncertainty of ~3%. The $X\,^1\Sigma^+(0^+)$ potential is adapted from Ref. 9 (see text for details) while the form of the $Y(0^+)$ potential remains preliminary.

	$X\,^1\Sigma^+(0^+)$	Eq. (8)	$A\,^3\Pi(1)$	Eq. (9)	$B\,^3\Pi(0^+)$	Eq. (9)
R_e	2.468 985 9857	Å	2.857 4784	Å	2.821 5300	Å
D_e	14 660[a]	cm^{-1}	2428	cm^{-1}	2314.8	cm^{-1}
T_e	−138[a]	cm^{-1}	12 370	cm^{-1}	16 168.4	cm^{-1}
γ			4.362 7716	$Å^{-1}$	4.937 3951	$Å^{-1}$
β_0	9.308 343 015					
β_1	17.902 504		4.441 061	$Å^{-1}$	5.100 9749	$Å^{-1}$
β_2	52.819 95		4.201 3071	$Å^{-2}$	6.074 5247	$Å^{-2}$
β_3	137.052		0.230 744 46	$Å^{-3}$	2.880 2781	$Å^{-3}$
β_4	244.33		0.384 948 62	$Å^{-4}$	11.463 025	$Å^{-4}$
β_5			7.100 1740	$Å^{-5}$	21.107 090	$Å^{-5}$
β_6			0.007 687 316	$Å^{-6}$	0.132 956 53	$Å^{-6}$
μ			0.236 D		0.635 D	
			$C\,^1\Pi(1)$	Eq.(10)	$Y(0^+)$	Eq. (10)
R_1			1.443 9470	Å	0	Å
b_1			9.119 5944	$Å^{-1}$	5.351 0378	$Å^{-1}$
A_1			$3.237\,559\,7\times10^7$	cm^{-1}	$8.016\,516\,78\times10^9$	cm^{-1}
R_2			0.068 986 47	Å	0	Å
b_2			1.760 4932	$Å^{-1}$	1.615 5024	$Å^{-1}$
A_2			$3.227\,961\,9\times10^5$	cm^{-1}	$3.557\,8710\times10^5$	cm^{-1}
T_e			14 798	cm^{-1}	14798	cm^{-1}
μ			0.480 D		0.0 D	

[a]The D_e value given by Ref. 9 underestimates the precise value of 14 798 cm^{-1} (Ref. 10). This has been compensated for by lowering the entire X state potential using the T_e term (see text).

tially derived from the corresponding partial absorption using the reflection principle. This trial potential was then used in a grid-based time-dependent wave packet calculation[47] of the frequency dependent partial absorption cross-section, $\sigma_{j-X}(\nu)$. A separate calculation was run for each level with $v'' \leqslant 3$. Details of these calculations are reserved until the following section, but each calculation involved wave packet propagation just for sufficient time that it had left the Franck–Condon region. The resulting absorption arising from the v'' level of interest was then determined from the Fourier transform of the autocorrelation function, $A(t)$, and the spectrum of the total partial absorption simply obtained as the sum of the different v'' contributions weighted appropriately for a 300 K vibrational state population distribution. The result, appropriately scaled vertically, was then compared with the experimentally determined partial absorption, $\sigma_{j-X}(\nu)$. The repulsive wall of the trial state potential was then adjusted, the wave packet propagation process repeated and, in this iterative way, the ''best-fit'' (by eye) potential function was eventually derived. Note that, implicit in this analysis and in the overall deconvolution that follows, is the assumption that all of the various electronic transition moments are R independent in the vertical Franck–Condon region of interest.

Defining the diabatic $B\,^3\Pi(0^+)$ state potential proved most challenging, both because of the fragmentary nature of the available vibrational term values, and because these are of course not eigenvalues of the diabatic B state potential but of the coupled B/Y system. As a starting point we used literature values for the inner, $R_{\min}$, and outer, $R_{\max}$, turning points for the lowest few B state vibrational levels ($v'=0$ and 2–4, i.e., well below the B/Y crossing) and $R_{\max}$ values for a selection of the better determined higher vibrational levels (v' from 11 to 34),[2] together with points in the Franck–Condon region, $T_e = 16\,168.4$ cm^{-1} (Ref. 7) and $D_e = 2315$ cm^{-1} (Ref. 10), and fitted them in terms of an extended Rydberg potential of the form:

$$V_B(R) = D_e\left[1 - \left(1 + \sum_{i=1}^{n} \beta_i (R - R_e)^i e^{-\gamma(R-R_e)}\right)\right] + T_e, \quad (9)$$

with R_e, β_i $(i \leqslant 6)$ and γ as adjustable parameters. Inclusion of the $R_{\max}$ values for the higher v' levels in the fit (albeit with a lower weighting) was necessary to provide some definition of the long range part of the potential. Figure 10 compares the experimentally determined and calculated partial cross-sections for parallel absorption $\sigma_{\text{par}}(\nu)$ (at 300 K), while the best-fit diabatic B state potential is shown in Fig. 11 and its best-fit potential parameters are listed in Table I. The nature and strength of the coupling between the diabatic B and Y states are considered later in this study, but modeling of the energies and widths of the resonance structure supported by the well of the diabatic B state potential is reserved for a future publication.[35]

As anticipated, Fig. 10 confirms that $\sigma_{\text{par}}(\nu)$ fails to account for both the high and low frequency ends of the total IBr visible absorption system. The missing absorption at the low frequency end of the spectrum we associate with the

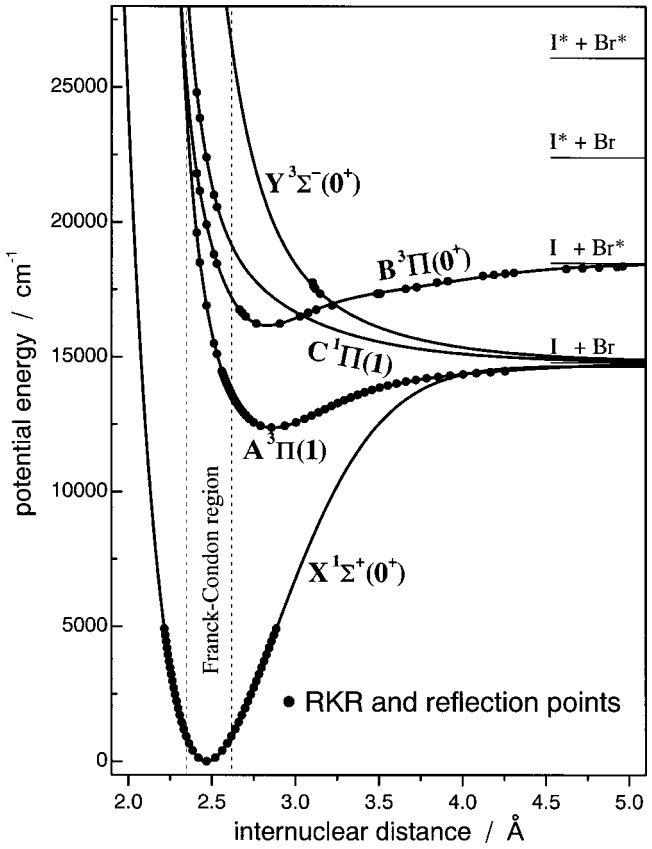

FIG. 11. Diabatic potential energy curves for the *X*, *A*, *B*, and *C* states of IBr derived in the present work. Also shown, for completeness, is the assumed location of the diabatic *Y* state potential responsible for the predissociation of the higher v' levels of the *B* state. RKR points are taken from a variety of sources as detailed in the text, while all relevant potential parameters are given in Table I.

$A-X$ transition. Appadoo *et al.*[6] provide Dunham coefficients for the bound part of the $A\,^3\Pi(1)$ state potential—at least up to $v'=24$ (corresponding to ~85% of the total *A* state well-depth), above which the $A-X$ absorption spectrum shows evidence of significant perturbation. These coefficients were used as input for an RKR calculation to generate turning points. The $A\,^3\Pi(1)$ state ''trial'' potential was again fitted in terms of an extended Rydberg potential [Eq. (9)], with $D_e=2428$ cm^{-1},[10] $T_e=12\,370$ cm^{-1} (Ref. 6), $R_e=2.8575$ Å as determined from the RKR fit, and $\beta_i(1\leqslant i\leqslant 6)$ and γ as adjustable parameters. The optimum *A* state potential and $\sigma_{A-X}(\nu)$ partial cross-section derived (following the procedures described above) are included in Figs. 11 and 10, respectively, while the parameters describing the best-fit extended Rydberg potential for the *A* state are listed in Table I.

Finally, the high frequency remainder of the 360–800 nm room temperature absorption band of IBr is attributed to the $C\,^1\Pi(1)\leftarrow X$ transition. To generate the *C* state potential we assumed a trial repulsive function of the form

$$V_C(R)=A_1\exp\{-b_1(R-R_1)\}+A_2\exp\{-b_2(R-R_2)\}+T_e \tag{10}$$

positioned in the vertical Franck–Condon region with parameters A_i, b_i, R_i, and T_e initially fitted to points in the Franck–Condon region derived by applying the reflection principle to the remaining high frequency part of the absorption. Fluorescence decay measurements[7] indicate that the $v'=2$ and 3 levels of the *B* state are affected by heterogeneous (rotational level dependent) predissociation caused by interaction with a dissociative state with $\Omega=1$. Analogy with other halogens suggests that the $C\,^1\Pi(1)$ state is responsible for the observed predissociation, while the absolute predissociation rates measured and their isotopic dependence suggests that the $B\,^3\Pi(0^+)/C\,^1\Pi(1)$ curve crossing occurs in the energetic vicinity of the $B_{v'=3}$ origin. This observation provides a further constraint when determining the most probable *C* state potential displayed in Fig. 11. Figure 10 illustrates how well the measured room temperature absorption spectrum is replicated by the three deduced partial absorption cross-sections, while Table I provides a summary of the functional form of each potential and of their respective transition moments, μ_{j-X}. Given the assumption that the various μ_{j-X} are independent of *R*, the uncertainty in the *relative* transition moments obtained from this deconvolution is judged to be ~1%. The reliability of the absolute values quoted in Table I depends upon the accuracy of the reported total absorption cross-sections—estimated to be $\sim\pm 2.5\%$ at the maximum absorption,[17] hence the ~3% uncertainty quoted in the caption to Table I. The value we obtain for μ_{B-X} (0.635 D) is in pleasing accord with the earlier value of 0.7 D estimated by Clyne and Heaven on the basis of their collision-free IBr ($B\rightarrow X$) fluorescence lifetime measurements and intercomparison with other halogens and interhalogens.[7]

The accuracy of the repulsive walls of the derived *A*, *B*, and *C* state potentials in the vertical Franck–Condon region is estimated to be $\sim\pm 50$ cm^{-1}. The bound part of the $A\,^3\Pi(1)$ state potential is accurate to the extent that the vibrational term values calculated from the Dunham coefficients of Ref. 6 reproduce the experimental energies with an average deviation of 0.3 cm^{-1}, with maximal differences of -0.7 cm^{-1} for the $v'=0$ level and $+1.1$ cm^{-1} for the highest valid vibrational level ($v'=24$). The long range part of the diabatic $B\,^3\Pi(0^+)$ state potential, and the repulsive $Y\,^3\Sigma^-(0^+)$ potential (see Sec. III E) remain less well-defined, pending a proper coupled treatment of the *B/Y* states in order to reproduce the structured, predissociated part of the absorption spectrum in the wave-number range 16 500–18 350 cm^{-1}.[35]

E. Wave packet calculations of $\Gamma(\nu)$ and $\beta(\nu)$

Grid-based time-dependent wave packet calculations of the visible photofragmentation of IBr have been performed as a further test of the accuracy of the derived excited state potential energy curves and transition dipole moments and to allow determination of the coupling strength between the diabatic *B* and *Y* states. The calculations involved solution of the time-dependent Schrödinger equation,

$$i\hbar\frac{\partial}{\partial t}\Phi(R,t)=\hat{H}(R)\Phi(R,t), \tag{11}$$

following procedures outlined elsewhere.[47] The time-dependent Hamiltonian, $\hat{H}(R)$, in the present calculations, is the sum of the radial nuclear kinetic energy operator, $\hat{T}(R)$, the diabatic potential energy, $V(R)$, and a coupling term, $V_{B/Y}$ (which we take to be R independent), linking the diabatic $B(0^+)$ and $Y(0^+)$ states. The calculations assume total angular momentum $J=0$ throughout. The starting point of these time-dependent calculations is the preparation of an initial wave packet on each of the *A*, *B*, and *C* state potential energy curves. These are obtained by multiplying the ground state wave function $\Psi_{v''}$, itself determined using the Fourier grid Hamiltonian method,[48] by the appropriate transition moment function, i.e.,

$$\begin{pmatrix} \Phi_A(R,t=0) \\ \Phi_B(R,t=0) \\ \Phi_C(R,t=0) \\ \Phi_Y(R,t=0) \end{pmatrix} = \begin{pmatrix} \mu_{A-X}\Psi_{v''}(R) \\ \mu_{B-X}\Psi_{v''}(R) \\ \mu_{C-X}\Psi_{v''}(R) \\ 0 \end{pmatrix}. \tag{12}$$

$\Phi_j(R,t)$ represents the wave packet associated with the electronically excited state j and μ_{j-X} (assumed to be R independent) is the transition moment connecting state j with the ground electronic state. Separate calculations are run for each ground state vibrational level with $v''\leqslant 3$. The various $\Phi_j(R,t=0)$ wave packets are propagated on the relevant excited state potential(s) in a series of short time steps using the Chebychev propagation scheme[49,50] and the respective autocorrelation functions $A_j(t)$ are calculated:

$$A_j(t)=\int_0^\infty \Phi_J^*(R,t=0)\Phi_j(R,t)dR. \tag{13}$$

Partial absorption cross-sections $\sigma_{j-X}(\nu)$, such as those shown in Fig. 10, are obtained by Fourier transforming the various $A_j(t)$:

$$\sigma_{j-X}(\nu)=\frac{\pi\nu}{3c\epsilon_0\hbar}\int_{-\infty}^{\infty}\exp[i(E_{v''}+h\nu)t/\hbar)]A_j(t)dt, \tag{14}$$

where $E_{v''}$ is the vibrational energy of the initial state, and then summing contributions associated with the different v'' levels weighted appropriately for a 300 K vibrational state population distribution. In practice, since the first aim of the preceding calculations was simply to define the short range repulsive parts of the *A*, *B*, and *C* state potentials, it was only necessary to propagate each wave packet until it had departed from the vertical Franck–Condon region. These $\sigma_{j-X}(\nu)$ calculations were thus insensitive to the assumed form and strength of any coupling between the *B* and *Y* state diabatic potentials at larger *R*.

Clearly, such will not be the case when we turn to consider the partial cross-sections for forming a particular asymptotic product state. These are obtained by examining the wave packets associated with each of the *four* excited state potentials at an analysis line at large $R=R_\infty$, in the asymptotic region where there is no further coupling between the diabatic surfaces. The partial cross-section, $\sigma_j(\nu)$, for forming a given product channel j is given by[47]

$$\sigma_j(\nu)=\left(\frac{4\pi^3\nu k}{3c\epsilon_0\mu}\right)|A_j(R_\infty,E)|^2, \tag{15}$$

TABLE II. Numerical parameters of the time-dependent wave packet calculations for $I^{79}Br$. Note that the results for the $I^{79}Br$ and $I^{81}Br$ isotopomers are indistinguishable.

Atomic masses	m_I	126.904 473 amu
	m_{Br}	78.918 3361 amu
Range of grid	R_{min}, R_{max}	4.0–24.0 Bohr
Number of grid points		1024
Position of analysis line	R_∞	19.5 Bohr
Time step	δt	0.483 78 fs
Number of time steps		8192
Start of damping region	R_{damp}	20.0 Bohr
Cubic damping factor (Ref. 51)	C_{damp}	0.010 41 Hartree

where

$$A_j(R_\infty,E)=\frac{1}{2\pi}\int_0^\infty \Phi_j(R_\infty,t)\exp[i(E_{v''}+h\nu)t/\hbar]dt, \tag{16}$$

k_j is the wave vector of the photofragments and μ is their reduced mass. For these calculations, the asymptotic wave functions were damped using a cubic complex absorbing potential as defined by Eq. (11) of Ref. 51 in order to prevent spurious recurrences at small *R*. Table II gives values of all parameters, including the damping parameters, used in the final time-dependent wave packet calculations.

Recalling Fig. 11, we note that, for the four state model used here, the diabatic *A*, *C*, and *Y* state potentials correlate smoothly with ground state I+Br products, while the spin-orbit excited I+Br* asymptote connects with just the diabatic *B* state potential. In the absence of any heterogeneous couplings, wave packets propagated on the *A* and *C* state potentials thus evolve solely to ground state products, which will show perpendicular recoil anisotropy. Wave packets launched on the *B* state potential, however, will bifurcate in the region where this potential crosses with that of the diabatic *Y* state, to an extent that will depend on the strength of the *B/Y* coupling. Given independent knowledge of the form of the *A*, *B*, and *C* state potentials, and the respective transition moments connecting each of these states with the ground state, the shape of the *Y* state potential and $V_{B/Y}$, the strength of its coupling to the *B* state, are the only adjustable parameters in modeling the observed energy dependent branching ratio, Γ, and produce recoil anisotropies, β.

The dissociation limit of the diabatic *Y* state potential, and the approximate energy at which it crosses that of the diabatic *B* state are both known from experiment. Further refinement of its shape at shorter *R* must await more detailed analysis and interpretation of the short lived resonances supported by the diabatic *B* state well, but for the present purposes, its representation in terms of a potential analogous to that used to describe the repulsive *C* state [Eq. (10)], with parameters as listed in Table I, suffices to reproduce the experimental measurables. Figure 11 displays the form of the assumed diabatic *Y* state potential, while Fig. 12 shows the frequency dependent branching fraction for Br* products

$$\Gamma(\nu)=\frac{\langle\sigma_B(\nu)\rangle}{\left\langle\sum_j \sigma_j(\nu)\right\rangle}, \tag{17}$$

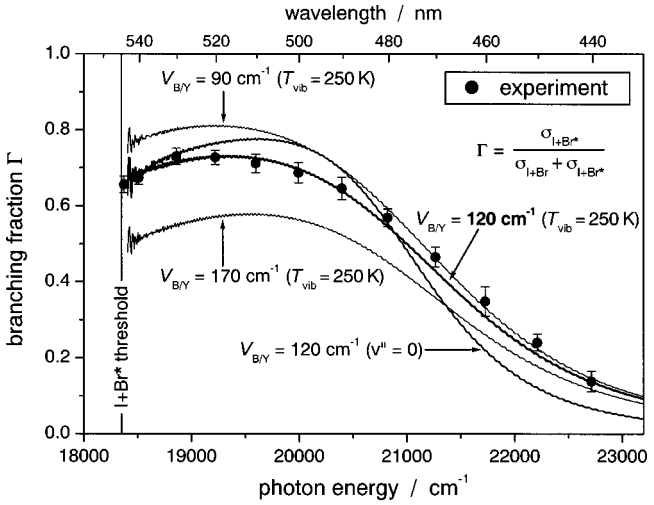

FIG. 12. Comparison of experimentally determined Br* product branching fractions $\Gamma(\nu)$, (●), with those derived from analysis of wave packets reaching the R_∞ analysis line at the I+Br* and I+Br asymptotes, assuming a parent vibrational temperature of $T_{\text{vib}}=250$ K and different *B/Y* coupling constants: $V_{B/Y}=170$, 120, and 90 cm^{-1}. The parameters and respective transition moments of the excited state potentials are given in Table I. Also shown, as a dashed line (– – –), is the $\Gamma(\nu)$ curve predicted in the case that the parent sample consisted solely of molecules with $v''=0$.

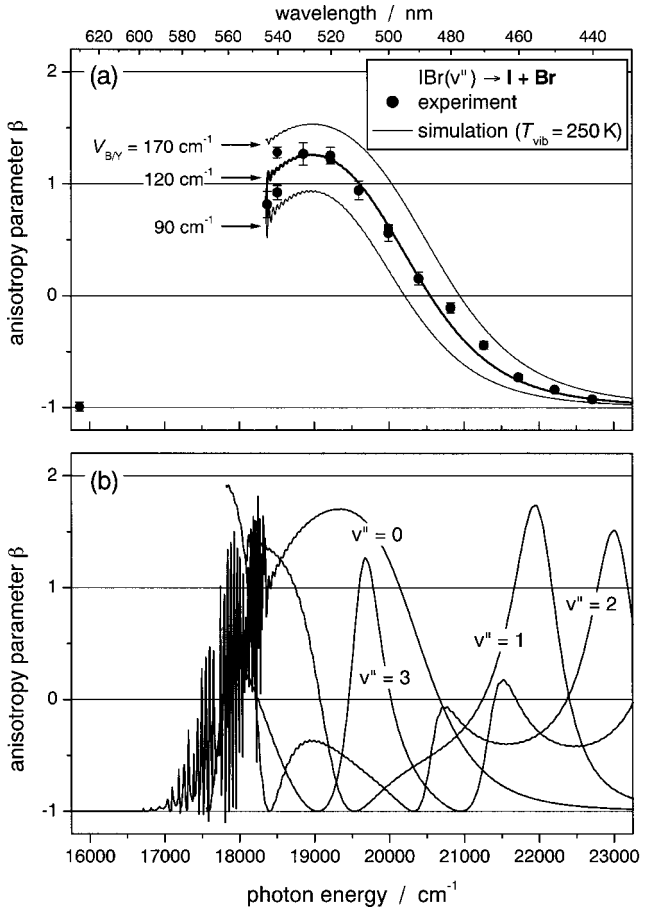

FIG. 13. (a) Comparison between the experimentally determined β parameters for the I+Br product channel as a function of photolysis wavelength, with the (vibrationally averaged) results of wave packet calculations assuming $V_{B/Y}=170$, 120, and 90 cm^{-1}. (b) Calculated frequency dependent variation of the I+Br product recoil anisotropy, assuming $V_{B/Y}=120$ cm^{-1}, following photolysis of vibrationally state selected IBr molecules with $v''=0$, 1, 2, and 3. The rapid oscillatory structure at $h\nu<18\,350$ cm^{-1} reflects the predissociation of bound *B* state levels by coupling to the *Y* state (shown for $v''=0$ only).

determined at the R_∞ analysis line, assuming a parent vibrational temperature of 250 K (from hereon the $\langle\,\rangle$ brackets will be used to imply vibrationally averaged quantities) and three different values of $V_{B/Y}$: 170 cm^{-1}—as estimated in the original analysis of Child;[2] 90 cm^{-1}—as assumed in many of the more recent theoretical studies of IBr photophysics;[14–16] and 120 cm^{-1}. The latter represents our best-fit value (by eye) and, as Fig. 12 demonstrates, it reproduces the experimentally determined branching fraction very well indeed. Also shown in Fig. 12 are the results of the wave packet calculations for parent IBr molecules in just their ground vibrational state. These serve to illustrate the sensitivity of $\Gamma(\nu)$ to the parent vibrational temperature.

As Fig. 13 shows, the wave packet calculations with $V_{B/Y}=120$ cm^{-1} are equally successful at reproducing the form of the experimentally measured energy dependence of the recoil anisotropies. Within the confines of the potentials shown in Fig. 11, only that part of the wave packet launched on the diabatic *B* state potential that remains on this potential will reach the analysis line at the I+Br* asymptote. Since the initial excitation involves a $\Delta\Omega=0$ transition, the prediction that the I+Br* products will display an angular anisotropy characterized by $\beta=+2$ at all excitation wavelengths is trivial and is therefore not shown in Fig. 13. In contrast, the diabatic potentials of the *A*, *C*, and *Y* states all converge to the I+Br asymptote. The two former potentials are both reached via a perpendicular transition from the $X\,^1\Sigma^+(0^+)$ state, and flux evolving on these two potentials is assumed to exhibit a recoil anisotropy characterized by an anisotropy parameter, $\beta=-1$. Flux reaching the I+Br dissociation limit on the diabatic *Y* state potential will have transferred to it after initial excitation to the $B(0^+)$ potential via a parallel transition; this flux will recoil with an angular distribution characterized by $\beta=+2$. In terms of the foregoing, $\beta_{\text{Br}}(\nu)$ will thus be given by [cf. Eq. (7a)]

$$\beta_{\text{Br}}(\nu)=\frac{2\langle\sigma_Y(\nu)\rangle-\langle\sigma_A(\nu)\rangle-\langle\sigma_C(\nu)\rangle}{\langle\sigma_Y(\nu)\rangle+\langle\sigma_A(\nu)\rangle+\langle\sigma_C(\upsilon)\rangle}. \tag{18}$$

Figure 13(a) illustrates how well the experimentally measured β parameter for the I+Br products, and its frequency dependence, are reproduced by Eq. (18), after vibrational averaging, assuming $V_{B/Y}=120$ cm^{-1}.

Analysis of images recorded following photolysis at wavelengths in the range 540–490 nm suggested that the recoil anisotropy of the I+Br products was sensitive to the initial vibrational state of the parent molecule [recall, for example, Fig. 6 and Fig. 7(b)]. The wave packet calculations provide a rationale for this observation. Figure 13(b) shows plots of calculated $\beta_{\text{Br}}(\nu)$ values following photolysis of IBr molecules in selected initial v'' states. Clearly, each shows its own distinctive dependence on excitation frequency, reflecting (in a time-independent picture) the differing Franck–Condon overlaps of each v'' wave function with the transla-

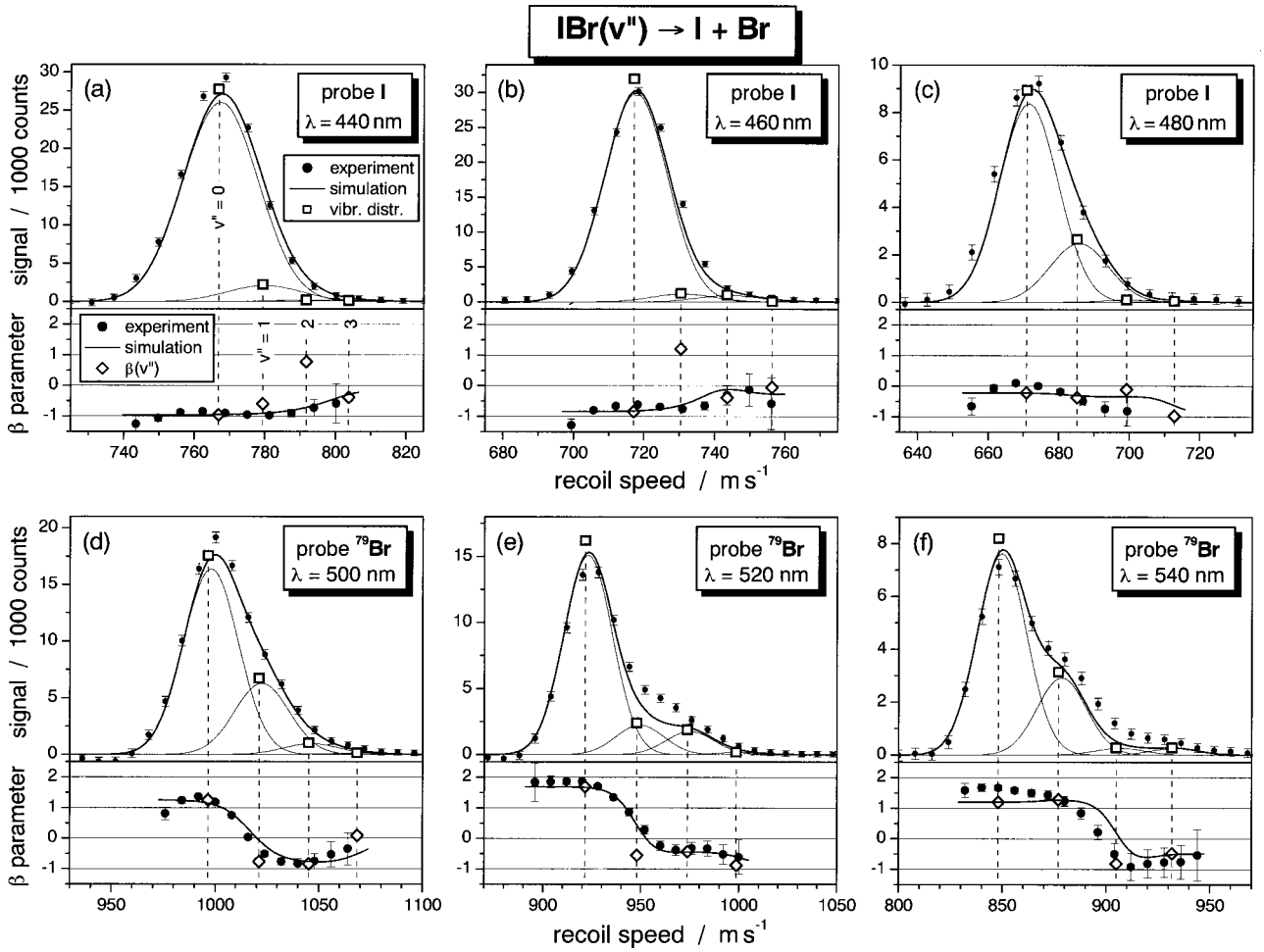

FIG. 14. Plot illustrating the variation in the recoil anisotropy of the I+Br products arising in the photolysis of IBr at (a) 440 nm, (b) 460 nm, and (c) 480 nm (monitoring I fragments), and at (d) 500 nm, (e) 520 nm and (f) 540 nm, (monitoring ^{79}Br atoms). As in Figs. 6 and 7, the upper and lower parts of each panel show, respectively, the signal intensity and the derived β parameter as a function of pixel radius (and thus recoil velocity). The experimental data points are shown as filled circles (●, with $\pm 1\sigma$ error bars). Both, the signal intensity and the β parameters were also simulated (solid lines, shown only at velocities where signal is observed) using the partial cross sections for formation of I+Br products resulting from photolysis of IBr ($v''=0-3$) parent molecules (□) and β parameters (◇) derived from the wave packet calculations (assuming $T_{\mathrm{vib}}=250$ K). The simulations take into account the experimental resolution as well as the parent rotational state population distribution for $T_{\mathrm{rot}}=12$ K (see text).

tional wave functions associated with the *A*, *B*, and *C* state potentials. In the case of IBr($v''=0$) molecules, for example, β_{Br} is predicted to vary from strongly positive at ~520 nm (reflecting the dominance of the *B*–*X* transition moment in this wavelength region) to near limiting −1 at the shortest excitation wavelengths (where, for these molecules, the *C* ←*X* excitation is pre-eminent). Capturing the detailed v'' dependence and wavelength dependence of the experimentally measured β_{Br} values should provide a stringent test of the accuracy of the excited state potentials (particularly their repulsive parts) derived in this study.

Figure 14 illustrates the good agreement between the experimentally measured velocity dependent I+Br signal strengths and angular anisotropies, measured at six photolysis wavelengths in the range 440–540 nm, and the results of the wave packet calculations. Each spectrum was first fitted as outlined in Sec. II in order to establish the pixel→velocity scaling factors and the widths of the associated model functions. The spectra are then simulated using the relative signal strengths from each parent v'' vibrational level given by the wave packet calculations (indicated by □ in the upper half of each panel in the figure) rather than the values determined by the fitting procedure. As Fig. 14 illustrates, the shapes of the intensity profiles are reproduced well, with only some minor discrepancies at the longer photolysis wavelengths. To simulate the variations of the anisotropy parameter with recoil speed, the β parameters taken from the wave packet calculations (Fig. 13) had to be convoluted by the model function and weighted according to the relative signal strengths associated with each parent v'' level (shown by ◇ in the lower part of each panel of Fig. 14). Again, the wave packet calculations quantitatively reproduce the v'' (and thus recoil velocity) dependent variation in β observed at each wavelength, and the way in which β varies with excitation wavelength. They also serve to highlight, once again, the potential pitfalls that can arise when interpreting experimentally measured β parameters, even in the case of monochromatic photolysis of a diatomic molecule. Clearly, in the present case, the β value so derived will depend on the energy resolution of the analysis and the vibrational state population distribution in the parent molecular beam.

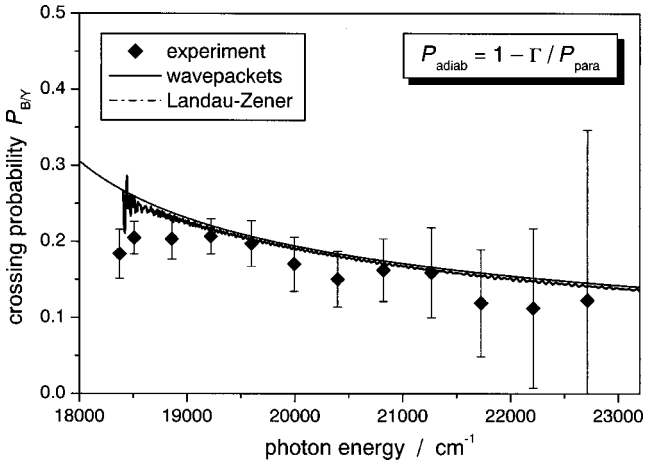

FIG. 15. Plot showing the probability of *B/Y* curve crossing derived from experiment (◆, with $\pm 1\sigma$ error bars), from the wave packet calculation (—) and from the Landau–Zener model (–·–·–) (see text). The theoretical predictions are an average over v'' appropriate for a vibrational temperature $T_{vib} = 250$ K.

F. Diabatic versus adiabatic description of IBr photolysis

The preceding discussion, couched entirely in terms of diabatic potentials and a coupling parameter $V_{B/Y}$, successfully reproduces all of the experimental measurables. Thus it is both possible and instructive to determine the fraction of molecules initially excited to the *B* state potential which dissociate *diabatically* (to I+Br*) and those which follow the *adiabatic* route, transferring to the diabatic *Y* potential and yielding I+Br products. The diabatic fraction, P_{diab}, can be deduced from the experimental measurements as the ratio

$$P_{diab} = \frac{\Gamma}{P_{par}}, \tag{19}$$

where, as before, P_{par} [Eq. (7a)], is the fraction of the total absorption that populates the *B* state and Γ [Eq. (4)] gives the fraction of that population that follows the diabatic *B* state potential to the I+Br* dissociation limit. The fraction of *B* state molecules that follow the adiabatic path, P_{adiab}, is then simply given by $(1 - P_{diab})$. Figure 15 shows the experimentally derived crossing probabilities from the diabatic *B* state potential to the *Y* state, as a function of excitation wavelength, to be in excellent accord with the results from the wave packet calculations. P_{adiab} emerges from the latter in a most transparent manner, simply as

$$P_{adiab} = \frac{\langle \sigma_Y(\nu) \rangle}{\langle \sigma_B(\nu) \rangle + \langle \sigma_Y(\nu) \rangle}, \tag{20}$$

where, as before, $\langle \sigma_B(\nu) \rangle$ and $\langle \sigma_Y(\nu) \rangle$ are respectively, the branching ratios for forming Br* and Br atoms following an initial parallel absorption event, suitably averaged for a 250 K parent vibrational state population distribution, analyzed at R_∞.

As Fig. 15 also shows, both the magnitude and the frequency dependence of P_{adiab} can be reproduced well using a Landau–Zener based model. Following Child,[2] we can define

$$P_{adiab} = 1 - \exp\left[\frac{2\pi V_{B/Y}^2}{\hbar v(E) \Delta F}\right], \tag{21}$$

where the velocity v is defined by

$$\tfrac{1}{2}\mu\{v(E)\}^2 = E - E_x. \tag{22}$$

E is the photon energy, and E_x and ΔF are, respectively, the energy at the point of intersection between the diabatic *B* and *Y* state potentials and the difference between the slopes of these two potentials at this point. Given the *B* and *Y* state potentials shown in Fig. 11, $E_x = 16\,980$ cm^{-1} and $\Delta F = 6424$ cm^{-1} Å^{-1}. As Fig. 15 shows, these values together with the best-fit coupling strength, $V_{B/Y} = 120$ cm^{-1}, successfully reproduce the observed frequency dependence of P_{adiab}. Here it is worth reemphasizing the inter-dependence between $V_{B/Y}$ and the assumed forms of the diabatic *B* and *Y* state potentials, neither of which are, as yet, uniquely determined. Any subsequent refinement of these potentials, such as could emerge from a thorough analysis of the predissociated resonances supported by the diabatic *B* state potential, will map directly into the best-fit value of $V_{B/Y}$. We also note, however, that the spread of $V_{B/Y}$ values suggested by previous authors[2,14–16] is only partially explicable in terms of the differences in the assumed forms of these potentials.

IV. CONCLUSIONS

Careful, high resolution ion imaging studies of the visible photodissociation of jet-cooled IBr molecules have enabled determination of the branching into ground (I+Br) and spin-orbit excited (I+Br*) product channels, and the recoil anisotropy of both sets of products, as a function of excitation frequency. Analysis of such data has allowed decomposition of the essentially structureless parent absorption profile into frequency dependent partial cross-sections for parallel ($\Delta\Omega = 0$) and perpendicular ($\Delta\Omega = \pm 1$) excitation. These absorptions are attributable to transitions from the $X\,^1\Sigma^+(0^+)$ ground electronic states to the repulsive limbs of the diabatic potentials associated with the $A\,^3\Pi(1)$, $B\,^3\Pi(0^+)$, and $C\,^1\Pi(1)$ excited states of IBr. Comparison of these experimentally determined partial cross-sections with the output of complementary time-dependent wave packet calculations has allowed determination of the detailed form of the repulsive parts of each of these potentials in the vertical Franck–Condon region, and of the (*R* independent) transition moments to each of these excited states. These data, when combined with existing knowledge from bound state spectroscopy (in the case of the *A* and *B* states),[2–7] provide the most precise parametrization of these excited state potentials yet available. Further wave packet propagations on these diabatic potentials for the *A*, *B*, and *C* states, which allow for possible transfer of flux between the diabatic potentials of the *B* state and the repulsive $Y(0^+)$ state (which show a weakly avoided crossing at larger *R*, for which we determine a coupling matrix element $V_{B/Y} = 120$ cm^{-1}), successfully reproduce *all* experimentally determined quantities. These include: the frequency dependence of the total absorption cross-section, the product spin-orbit branching ratio, and the recoil anisotropies of each product channel; the relative probabilities of diabatic (i.e., to

I+Br*) versus adiabatic (to I+Br) fragmentation of IBr molecules following excitation to the $B(0^+)$ state at energies above the dissociation limit for the spin-orbit excited products; even the velocity dependence of the β parameter measured for the I+Br products formed at any one photolysis wavelength—a consequence of the fact that our IBr molecular beam contains parent molecules with $v'' \leqslant 3$ and, at any chosen excitation wavelength, these different vibrational levels can exhibit very different Franck–Condon overlaps with the various excited state potentials. The present work provides a further cautionary notice of the underlying complexity that may need to be understood before offering any meaningful interpretation of an experimentally measured β parameter, even in the case of a diatomic molecular dissociation. As shown here, and previously,[10] it also serves to demonstrate the substantial shortcomings in the previously reported model[2,11,12,14–16] and recent *ab initio*[52] potentials for IBr, including those which served to inspire past proposals for coherent control of IBr photodissociation following excitation via the $A\,^3\Pi(1)$ excited state.[26]

ACKNOWLEDGMENTS

Funding from the EPSRC (equipment grants, and a Senior Research Fellowship to M.N.R.A.), the Commission of the European Union [TMR Fellowship to E.W. and E.R.W. under Contract No. ERB-4061-PL-97-0264 (IMAGINE) and Erasmus scholarships to S.L. and S.S.], and the Royal Society is gratefully acknowledged. We are also very grateful to Bristol colleagues Professors G. G. Balint-Kurti, and R. N. Dixon, Dr. C. M. Western, M. Beckert, W. H. Howie, C. Murray and K. N. Rosser, to Professors M. S. Child (University of Oxford) and O. S. Vasyutinskii (Ioffe Institute, St. Petersburg), and to T. Berg and Dr. A. T. J. B. Eppink (LaVision) for their many important and varied contributions to the work described herein.

[1] M. S. Child and R. B. Bernstein, J. Chem. Phys. **59**, 5916 (1973).
[2] M. S. Child, Mol. Phys. **32**, 1495 (1976); and private communication.
[3] W. G. Brown, Phys. Rev. **42**, 355 (1932).
[4] L.-E. Selin, Ark. Fys. **21**, 479, 529 (1962).
[5] L.-E. Selin and B. Soderborg, Ark. Fys. **21**, 515 (1962).
[6] D. R. T. Appadoo, P. F. Bernath, and R. J. LeRoy, Can. J. Phys. **72**, 1265 (1994).
[7] M. A. A. Clyne and M. C. Heaven, J. Chem. Soc., Faraday Trans. 2 **76**, 49 (1980).
[8] E. M. Weinstock, J. Mol. Spectrosc. **61**, 395 (1976).
[9] B. Nelander, V. Sablinskas, M. Dulick, V. Braun, and P. F. Bernath, Mol. Phys. **93**, 137 (1998).
[10] E. Wrede, S. Laubach, S. Schulenburg, A. J. Orr-Ewing, and M. N. R. Ashfold, Chem. Phys. Lett. **326**, 22 (2000).
[11] I. Levy, M. Shapiro, and A. Yogev, J. Chem. Phys. **96**, 1858 (1992).
[12] H. Guo, J. Chem. Phys. **99**, 1685 (1993).
[13] E. A. Volkers, A. E. Wiskerke, R. Mooyman, M. J. J. Vrakking, and S. Stolte, Phys. Chem. Commun. http://www.rsc.org/ej/qu/2000/b006982p/index.htm
[14] M. J. J. Vrakking, D. M. Villeneuve, and A. Stolow, J. Chem. Phys. **105**, 5647 (1996).
[15] M. Shapiro, M. J. J. Vrakking, and A. Stolow, J. Chem. Phys. **110**, 2465 (1999).
[16] A. N. Hussain and G. Roberts, J. Chem. Phys. **110**, 2474 (1999).
[17] D. J. Seery and D. Britton, J. Phys. Chem. **68**, 2263 (1964).
[18] G. E. Busch, R. T. Mahoney, R. I. Morse, and K. R. Wilson, J. Chem. Phys. **51**, 837 (1969).
[19] M. S. de Vries, N. J. A. van Veen, and A. E. de Vries, Chem. Phys. Lett. **56**, 15 (1978).
[20] M. S. de Vries, N. J. A. van Veen, M. Hutchinson, and A. E. de Vries, Chem. Phys. **51**, 159 (1980).
[21] A. B. Petersen and I. W. M. Smith, Chem. Phys. **30**, 407 (1978).
[22] H. K. Haugen, A. Weitz, and S. R. Leone, J. Chem. Phys. **83**, 3402 (1985).
[23] H. Bony, M. Shapiro, and A. Yogev, Chem. Phys. Lett. **107**, 603 (1984).
[24] R. L. Pastel, G. D. Hagard, H. C. Miller, and S. R. Leone, Chem. Phys. Lett. **183**, 565 (1994).
[25] R. L. Pastel, J. K. McIver, H. C. Miller, and G. D. Hager, J. Chem. Phys. **100**, 3624 (1994).
[26] I. Levy, M. Shapiro, and P. Brumer, J. Chem. Phys. **93**, 2493 (1990).
[27] K.-W. Jung, J. A. Griffiths, and M. A. El-Sayed, J. Chem. Phys. **103**, 6999 (1995).
[28] Y. S. Kim, Y. J. Jung, and K. H. Jung, J. Chem. Phys. **107**, 3805 (1997).
[29] W. S. McGivern, R. Li, P. Zou, T. Nguyen, and S. W. North, Chem. Phys. **249**, 237 (1999).
[30] A. J. R. Heck and D. W. Chandler, Annu. Rev. Phys. Chem. **46**, 335 (1995).
[31] P. L. Houston, J. Phys. Chem. **100**, 12757 (1996).
[32] A. T. J. B. Eppink and D. H. Parker, Rev. Sci. Instrum. **68**, 3477 (1997).
[33] M. J. Cooper, P. J. Jackson, L. J. Rogers, A. J. Orr-Ewing, M. N. R. Ashfold, and B. J. Whitaker, J. Chem. Phys. **109**, 4367 (1998).
[34] M. J. Cooper, E. Wrede, A. J. Orr-Ewing, and M. N. R. Ashfold, J. Chem. Soc., Faraday Trans. **94**, 2901 (1998).
[35] E. Wrede, W. H. Howie, M. Beckert, E. R. Wouters, A. Brown, A. J. Orr-Ewing, and M. N. R. Ashfold (in preparation).
[36] M. N. Szilagyi, Proc. IEEE **73**, 412 (1985).
[37] Y. Sato, Y. Matsumi, M. Kawasaki, K. Tsukiyama, and R. Bersohn, J. Phys. Chem. **99**, 16307 (1995).
[38] A. S. Bracker, E. R. Wouters, A. G. Suits, Y. T. Lee, and O. S. Vasyutinskii, Phys. Rev. Lett. **80**, 1626 (1998).
[39] T. P. Rakitzis, S. A. Kandel, A. J. Alexander, Z. H. Kim, and R. N. Zare, J. Chem. Phys. **110**, 3351 (1999).
[40] P. C. Samartzis, B. L. G. Bakker, T. P. Rakitzis, D. H. Parker, and T. N. Kitsopoulos, J. Chem. Phys. **110**, 5201 (1999).
[41] A. S. Bracker, E. R. Wouters, A. G. Suits, and O. S. Vasyutinskii, J. Chem. Phys. **110**, 6749 (1999).
[42] Z. H. Kim, A. J. Alexander, S. A. Kandel, T. P. Rakitzis, and R. N. Zare, Faraday Discuss. **113**, 27 (1999).
[43] Y.-J. Jung, Y. S. Kim, W. K. Kang, and K.-H. Jung, J. Chem. Phys. **107**, 7187 (1997).
[44] R. N. Zare, *Angular Momentum. Understanding Spatial Aspects in Physics and Chemistry* (Wiley, New York, 1988).
[45] E. Wrede, M. N. R. Ashfold, and R. N. Dixon (in preparation).
[46] L. D. A. Siebbeles, M. Glass-Maujean, O. S. Vasyutinskii, J. A. Beswick, and O. Roncero, J. Chem. Phys. **100**, 3610 (1994).
[47] P. M. Regan, D. Ascenzi, A. Brown, G. G. Balint-Kurti, and A. J. Orr-Ewing, J. Chem. Phys. **112**, 10259 (2000) and references therein.
[48] C. C. Marston and G. G. Balint-Kurti, J. Chem. Phys. **91**, 3571 (1989).
[49] H. Tal-Ezer and R. Kosloff, J. Chem. Phys. **81**, 3967 (1984).
[50] R. Kosloff, J. Phys. Chem. **92**, 2087 (1988).
[51] Á. Vibók and G. G. Balint-Kurti, J. Phys. Chem. **96**, 8712 (1992).
[52] J. Pittner and P. Jungwirth, Chem. Phys. Lett. **321**, 281 (2000).